Continuum theory for confluent cell monolayers: Interplay between cell growth, division, and intercalation

Prakhar Bandil^a, Franck J. Vernerey^{1a}

^aDepartment of Mechanical Engineering, University of Colorado Boulder, U.S.A

Abstract

Mechanical forces generated by dynamic cellular activities play a crucial role in the morphogenesis and growth of biological tissues. While the influence of mechanics is clear, many questions arise regarding the way by which mechanical forces communicate with biological processes at the level of a confluent cell population. Some answers may be found in the development of mathematical models that are capable of describing the emerging behavior of a large population of active agents based on individualistic rules (single-cell response). In this perspective, the present work presents a continuum-scale model that can capture, in an average sense, the active mechanics and evolution of a confluent tissue with or without external mechanical constraints. For this, we conceptualize a confluent cell population (in a monolayer) as a deformable dynamic network, where a single cell can modify the topology of its neighborhood by swapping neighbors or dividing. With this description, we use concepts from statistical mechanics and the transient network theory to derive an equivalent active visco-elastic continuum model, which can recapitulate some of the salient features of the underlying network at the macroscale. Without loss of generality, the cell network is here assumed to follow well-known rules used in vertex model simulations, which are: (a) cell elasticity based on its bulk and cortical elasticity, (b) cell intercalation (or T1 transition), and (c) cell proliferation (expansion and division). We show, through examples and illustrations, that the model is able to characterize complex cross-talk between mechanical forces and biological processes, which are likely to drive the emergent growth and deformation of cell aggregates.

Keywords: Growth mechanics; Tissue viscoelasticity; Active materials; Statistical mechanics; Transient network theory

1. Introduction

Confluent cell ensembles are well-known to organize into a variety of architectures such as highly functional epithelial tissues, developmental embryonic tissues, and multi-cellular tumor spheroids. During development and disease, these cells are able to collectively grow, divide and reorganize, which can drastically change the aggregate size, architecture, and shape. These activities are orchestrated by a combination of biochemical signals, active force generation, and mechanical deformation that closely interact through feedback mechanisms (Gjorevski and Nelson, 2010); Heisenberg and Bellaïche, 2013). Deciphering how these cell-level interactions drive the long-term evolution of ensembles is at the heart of a number of biomedical applications across tissue engineering, organoid development, and oncology. At the same time, the development of accurate morpho-mechanic models (Montell, 2008); Friedl and Gilmour, 2009) is challenging for several reasons. First, the elasticity and long-term rheology of such active multicellular systems is highly nonlinear, time-dependent (Matoz-Fernandez et al., 2017); Kim et al., 2021; Duclut et al., 2022) and driven by active forces (Ladoux and Mège, 2017). Second, their mechanical response arises from diverse interacting factors (biological, chemical, physical) operating at different lengths and time scales (Wyatt et al., 2016). This includes glassy dynamics behavior (Schötz et al., 2013; Bi et al., 2016; Oswald et al., 2017) where they can transit from a fluid-like

¹correspondence to: franck.vernerey@colorado.edu

soft state to a solid-like jammed state. It is therefore necessary to concurrently consider the active mechanics of the cell cytoskeleton which operates at the sub-micron level (the deformation of single cells at the level of 1-10 microns) and finally the collective behavior of cells at the tissue level.

Cells in epithelial tissues are tightly bound via adherens molecules at the cell-cell interface endowing them with structural integrity as opposed to fluid-like embryonic tissues which lack mature adhesion junctions. Besides adhesion, the mechanical properties of these tissues are also ensured by the plasma membrane, the cytoplasm, and stresses generated within the actomyosin networks of the cell cortex and cell junctions. For instance, the cortical actomyosin networks, via their ability to generate localized and directed contractile stresses, are known to power cell division, polarization, and rearrangement (Montell) (2008). On the other hand, the junctional actomyosin networks are responsible for regulating the adhesion strengths at the junctions. In complement to experimental approaches, the agent-based models (or individual based models) (Osborne et al., 2017) have become important tools to better understand and quantify exactly how these cellular-level activities affect tissue development and mechanics (Wyczalkowski et al., 2012 Fletcher et al., 2017). Among them, the most prominent are particle-based models (Van Liedekerke et al., 2015), cellular Potts model (Szabó and Merks, 2013) and vertex models (Fletcher et al., 2014; Alt et al., 2017). Even though each one of them has its own strengths and limitations, the latter is particularly attractive for confluent cellular networks due to its ability to capture several physics (such as adhesion and contractility) and individual cell shapes in epithelial tissues. These models have been proven to explain phenomena such as wound healing (Tetley et al., 2019), rigidity transitions (Bi et al., 2015), cell proliferation (Farhadifar et al., 2007), as well as topological transformations (division, neighbor exchange, apoptosis and rosette transitions) (Staple et al., 2010) Yan and Bi, 2019) in epithelial sheets. With the advent of dynamic vertex models (Barton et al., 2017), the approach could be extended to out-ofequilibrium dynamics where the role of fluctuations (Sadati et al.) [2013) and cell polarity (Asnacios and Hamant, 2012) could be explored in systems such as tumors (Lin et al., 2017) or embryo development in the drosophila (Kong et al. [2017]. As with any modeling paradigm, the vertex model has its own limitations owing to its discrete and stochastic approach. These limitations mostly arise when considering tissues or organs made of a very large number of cells and in three dimensions. In this situation, the problem not only becomes computationally prohibitive (Fletcher et al., 2013) (although progress in high-performance computing may be a solution), but the dynamics become dominated by the law of large numbers. In other words, the mechanics of the large tissues is dominated by the average statistical response of the cell population.

On this end of the spectrum, continuum field theories offer an attractive mathematical framework, which lends itself to a deeper understanding of tissue dynamics. Continuum models have therefore been developed to describe tumor growth (Ambrosi and Mollica, 2004), tissue elasticity (Kupferman et al., 2020), rheology (Preziosi et al., 2010), and morphogenesis. These methods typically follow a top-down approach to derive constitutive relations from macroscopic observations, satisfying material symmetries and thermodynamic balance laws. Thus, by contrast to the bottom-up discrete approaches, the relationship between a continuum law and the underlying mechanisms is sometimes unclear. For instance, vertex simulations have shown that tissue rheology may arise from purely dissipative rearrangement mechanisms (Erdemci-Tandogan and Manning), [2021), but could alternatively be driven by active processes (Duclut et al., 2022). These may include, for instance, T1 transition propelling convergent extension (Zhou et al., 2015; Kong et al., 2017), or active stresses originating from cell division (Doostmohammadi et al., 2015). Similarly, continuum growth laws based on mixture theories (Humphrey, 2021) or the multiplicative decomposition of the deformation gradient tensor into elastic and growth components (Rodriguez et al., 1994; Lubarda and Hoger, 2002) successfully account for various macroscopic observations. However, they fall short in specifying the cellular processes at play. One such process of importance in biological growth is cell proliferation, which involves concurrent cell expansion and division. Although expansion and division are interconnected, they stem from distinct biological mechanisms, exerting disparate effects on growth dynamics. Existing continuum growth theories lack differentiation between these growth modes: increase in cell size versus increase in cell number. Additionally, during proliferation, cells, as seen in embryonic tissues, readily undergo rearrangements (neighbor exchange) (Jones and Chapman) (2012). Consequently, these models, treating tissue as behaving elastically over the growth timescale, prove inadequate for scenarios where rearrangements during growth could lead to viscous dissipation. To address these shortcomings and establish a deeper connection between macroscopic laws and cellular mechanisms, it is desirable to refine existing continuum models that are able to distinguish between tissue-level and cell-level deformation. A few models have

gone in this direction (Brodland et al.) 2006; Graner et al., 2008; Blanchard et al., 2009; Guirao et al., 2015; Tilil et al., 2015). One way to do so is by representing tissue configuration in terms of a mean cell with additional internal state variables containing cell-scale information. For instance, the model developed by Ishihara et al. (2017) is able to clearly link the mean cell conformation in epithelial tissues to their viscoelasticity and active behavior in response to T1 transitions. To the best of the authors' knowledge, this work was the first instance that combined ideas from the vertex model and a continuum-level model of tissues. Recently Staddon et al. (2023) also used the mean-field form of vertex models to explore the elastic behavior of epithelial tissues in detail. Even though hybrid continuum-discrete models (Van Liedekerke et al., 2015) have the potential to model complex tissue dynamics, most averaging techniques have primarily focused on capturing elastic behavior, with some consideration for the dissipative response. The investigation of tissue growth and cell proliferation has comparatively received less attention. Additionally, extending these theories into three dimensions faces practical challenges attributed to the mathematical formulation employed.

In the pursuit of advancing bottom-up methodologies (that are extendable to three dimensions), we here introduce a comprehensive continuum theory designed to model tissue growth and viscoelasticity based on the microscale kinematics of cell proliferation. To do this, we use the concepts of statistical mechanics with the objective of clearly linking the stochastic mechanics of a cell population to its macroscopic effective response. In solid mechanics, these concepts were originally developed by Flory and Rehner (1943) to describe the entropic elasticity of polymer networks. With the Transient Network Theory (TNT) (Tanaka and Edwards, 1992; Vernerey et al., 2017), the approach was then generalized to describe the viscoelasticity of networks with dynamic connections. The basic idea relies upon representing the discrete structure as a network whose elements possess an elastic component (elastic segment) and a time-dependent component, which enables the network to grow and change topology over time. Confluent cell ensembles do possess the attributes of a dynamic network, where nodes (representing cells) may exchange, create, or lose neighbors over time. The objective of the present work is therefore to employ ideas from statistical mechanics to construct a continuum theory for confluent cell ensembles, in which cells can undergo intercalation (T1 transitions), expansion, and division, three processes that are major players in tissue rheology, growth, and morphogenesis. For clarity and consistency with previous work, the model is constructed around the free energy and cellular-level rules delineated in the widely accepted vertex model. Given that vertex models are predominantly used for studying two-dimensional epithelial tissues, we confine this theory's application to confluent cell monolayers including cancer monolayers (Roshal et al., 2022). However, it is crucial to highlight that the model's adaptability to three dimensions is readily feasible and will be pursued in the near future.

The manuscript is organized as follows. In section 2 we provide a statistical description of a cellular network, corresponding statistical measures, and how they relate to cell conformation, which includes cell area and perimeter. Section 3 concentrates on the kinematics of a confluent cell population and their implication on the evolution of statistics over time. This yields a Fokker-Plank equation describing the evolution of the network's probability density. Section 3 concludes with a brief overview of thermodynamic formalism which sets the basis for not only deriving constitutive laws but also for providing deeper insights into the inelastic processes. Section 4 then focuses on the mechanics of the tissue by introducing the average elastic energy density of the cell population based on the vertex model. This allows us to introduce the average stress in the tissue. Section 5 then develops the inelastic models that arise from the considerations of inelastic processes, starting from the T1 transitions, cell division followed by proliferation which includes both - cell expansion and division. Illustrations of the resulting model are presented for simple boundary-value problems and compared with similar studies in the literature. Section 6 finally provides concluding remarks.

Table 1: Summary of important mathematical symbols used in this study

Туре	symbol	Meaning	Dimension
Vertex model quantities	$\mathcal E$	Free energy	J
	K	Cell area elasticity	N/m^3
	A_R	Preferred cell area	m^2
	L_R	Preferred cell perimeter	m
	$ar{\Gamma}$	Normalised cell contractility	1
	$ar{\Lambda}$	Normalised junction tension	1
	p_p	Preferred cell shape index	1
	e_0, σ_0	scaling factors for energy and stress	J, N/m
Cell population statistics	N	Number of cells	1
	r	Segment vector	m
	n	Number of segment vectors	1
	c	Nominal segment density	$1/m^{2}$
	C	Nominal cell density	$1/m^{2}$
	Ω	Segment conformation space	$m \times m$
	ϕ	Nominal segment distribution density	$1/m^4$
	p	Probability density function (pdf)	1
	M	Segment distribution covariance	m^2
	3	Confidence ellipse of <i>M</i>	
	A	Mean cell area	m^2
	L	Mean cell perimeter	m
	\mathcal{B}_0	Initial stress-free configuration	
Continuum model quantities	ζ_0	Residual volumetric elastic deformation	1
	\mathcal{B}_i	Intermediate stress-free configuration	
	ζ_i	Inelastic cell expansion ratio	1
	η	Cell number ratio	1
	${\mathcal B}$	Current deformed configuration	
	μ	Elastic deformation tensor	1
	ζ_e	Elastic volumetric deformation	1
	ζ	Dimensionless cell area	1
	ψ_i	Free-energy per unit area in \mathcal{B}_i	N/m
	ρ_i	Mass per unit area in \mathcal{B}_i	Kg/m^2
	D	Energy dissipation in tissue	J/s
	σ	Cauchy stress tensor	N/m
	ξ_c, ξ_l	Segment creation and loss rate	1/s, 1/s
	k_T, k_D, k_G	Rates for T1 transition, cell division and cell growth	1/s, 1/s, 1/s
	d_T, d_D, d_G	Inelastic flow rate tensors	1/s, 1/s, 1/s
	X	Cell shape anisotropy	1

2. Description of cell-networks

In an attempt to bridge cellular mechanisms to continuum scale, we opt for vertex models because, as we will see, they provide for a straightforward mapping between averaged constitutive laws and discrete-level rules governing stochastic effects and topological changes. Hence we start by briefly reviewing vertex models for epithelial tissues. This will then set the foundation for defining the confluent tissue configuration in various *deformed* and *physical* states in our model.

2.1. Discrete representation: vertex approach

Vertex models (Fletcher et al., 2013) 2014; Alt et al., 2017; Barton et al., 2017) make use of a simplified approximation in which cells within a confluent tissue can be mathematically represented as convex polygons. With this description (see Fig. []a.), three or more straight junctions meet a single point called the vertex. Despite certain efforts (Bock et al., 2010) that alleviate these geometric constraints (linear edges and polygon convexity) and capture more realistic cell shapes (Käfer et al., 2007), classical vertex models continue to effectively predict collective cell behavior. A

particularly attractive feature of these models is the introduction of a free energy functional \mathcal{E} that is expressed in terms of biophysical parameters and cell-level properties which include area A_I , perimeter L_I and junction length l_{IJ} where I and J denote cell indices. A coarse-grained estimation Ishihara et al. (2017); Staddon et al. (2023) of this energy functional can be made in terms of mean cell area $A = \langle A_I \rangle$ and mean cell perimeter $L = \langle L_I \rangle$ as:

$$\mathcal{E} \approx N \left[\frac{K}{2} (A - A_R)^2 + \frac{\Gamma}{2} L^2 + \frac{\Lambda}{2} L \right]$$
 (2.1)

where N is the total number of cells in the population. The first term arises from the cell's resistance to changes in its area and is expressed in terms of the cell's bulk modulus K and preferred area A_R . The second term represents the energy associated with the changes in the cell's perimeter, due to the combined elasticity Γ of the membrane and its underlying cortical actomyosin network. The third and last term finally characterizes the energy contribution from two competing factors, one the cell-cell adhesion mediated by E-cadherin junction molecules and the other junctional actomyosin networks, giving rise to a tension Λ at the cell-cell interface. Depending on which of the two dominates, the term Λ is affected as follows. A positive Λ implies that contractility in the junctional actomyosin networks dominates and cells work to decrease their contact area. In contrast, a negative Λ indicates that adhesion dictates, driving junction area expansion. The last two terms in eqn. (2.1) can also be interpreted as sources of surface tension forces as they regulate any changes in cell shape where Γ is responsible for cell-surface tension while Λ characterizes intercellular-surface tension (Lecuit and Lenne) (2007).

In the vertex models, the minimization of the above energy drives cell deformation and motion. In time, this energy may indeed change due to two mechanisms, which may be passive or active. Passive mechanisms merely arise from the application of external forces that could induce both elastic and inelastic tissue deformation. On the other hand, active mechanisms can be multiple and usually depend on the interplay between adhesion and contractile forces within the cells as well as in the junctions. Contractile forces that are generated by the junctional actomyosin structures (a layer of F-actin filaments and Myosin II motor proteins) control both the cortical elasticity Γ and bond tension A over time. Notably, bond tension can occur in a specific direction in order to coordinate anisotropic cell movement (Bertet et al., 2004; Zallen and Wieschaus, 2004; Rauzi et al., 2008). But cortical and junctional dynamics are not the only mechanisms that drive cell shape changes and their collective motion. Changes in preferred cell area A_R triggering growth and changes in cell polarity influencing migration patterns are some of the other forms of active mechanisms that can be modeled as per the vertex-based simulations (Barton et al.) [2017]. A variety of rules can be introduced in vertex models to observe the emerging behavior of epithelial tissues under various cellular processes. With an increase in system size, i.e. degrees of freedom, the amount of information can quickly become very large, which could sometimes, make it difficult to identify the governing factors for a given macroscopic response. To address this issue, we now develop a continuum model based on the reduced mean-field approximation of confluent cellular networks. Our objective in this context is not to propose an alternative to the vertex model, but rather to gain insights into how the cell-level events manifest in a continuous framework.

2.2. Statistical description: TNT approach

In this section, we employ a statistics-based approach to provide a novel interpretation of cell networks that is independent of individual cell geometries. Consider a two-dimensional macroscopic tissue domain B confined by boundary ∂B as shown in Fig. []b. An elementary area centered around a point with Lagrange coordinate X can be thought of to be composed of a large number, N(X,t), of confluent cells. This collection of N cells can be used to statistically describe the tissue structure at continuum point X. Following the transient network theory (TNT) (Vernerey et al., 2017), this collection may be viewed as a dynamic network (Fig. []b.) of cells whose nodes represent the geometric cell centers and segments, denoted by the vector \mathbf{r} , indicate a physical connection between two neighboring cells. Also, note that the segment vectors are apolar, i.e., their direction is randomly assigned such that, they can be written in terms of a magnitude $r = |\mathbf{r}|$ and a direction angle θ , resulting in $\mathbf{r} = [r_x, r_y] = [r\cos\theta, r\sin\theta]$. The total number n(X,t) of such segment vectors in the network is given by n = ca(0), where c(X,t) is the nominal density of segment vectors and a(0) is the *initial* elementary area at X. A statistical description of the cellular network may then be introduced by considering \mathbf{r} as a continuous random variable in virtual conformation space Ω (Fig. []c.) which is embedded within the Lagrangian point X. Theoretically, this conformation space Ω is an infinite space with segment vectors

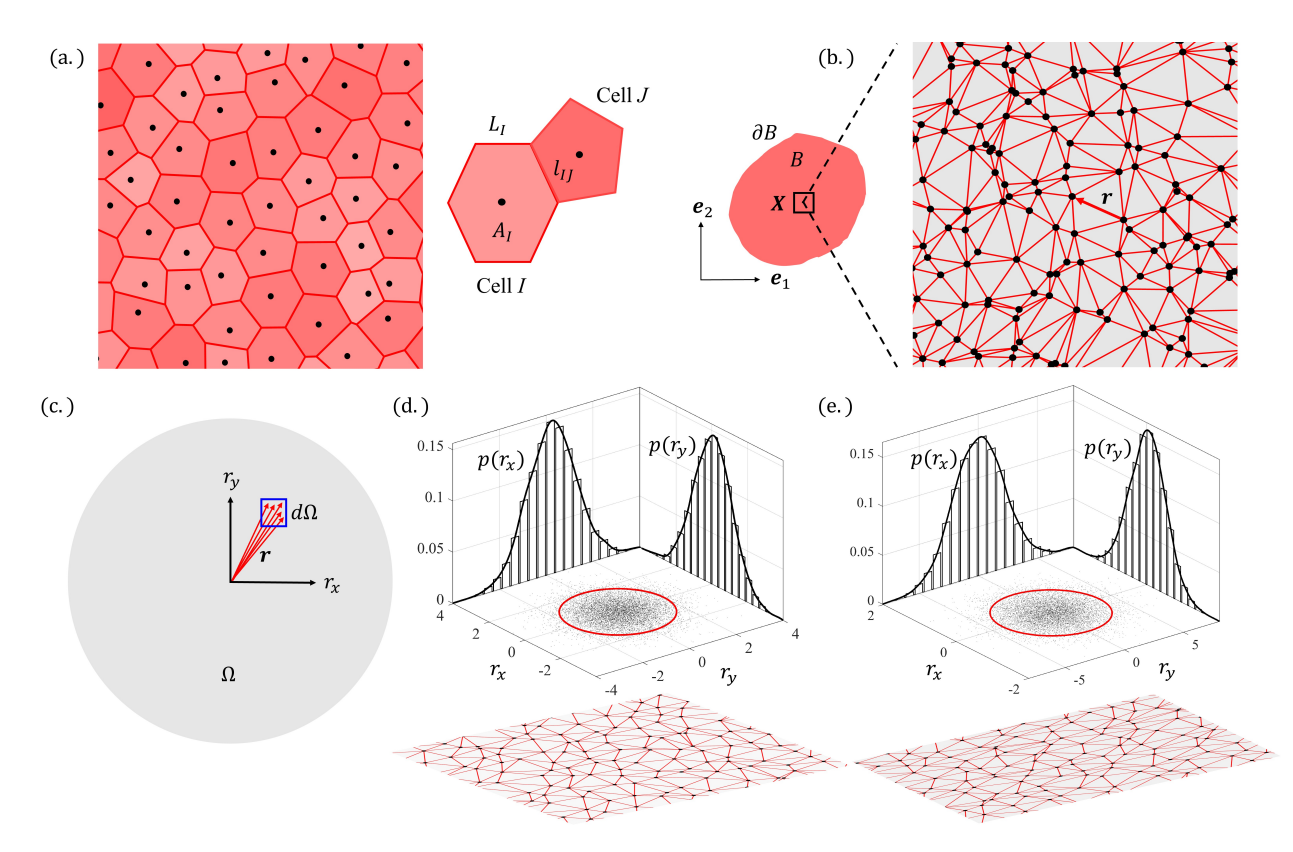


Figure 1: (a.) Vertex model representation as given by a unique polygonal tessellation, called Voronoi tessellation (b.) A network of confluent cells where nodes (solid black dots) correspond to the geometric cell centers and segments (solid red lines) connect adjacent cell centers. (c.) The network statistics is captured by the distribution of these center-to-center segment vectors in a *conformation space* $\Omega \in \mathbb{R}^2$ with bases $\{r_x, r_y\}$. The probability density function $p(r_x, r_y)$ of this distribution is depicted as a confidence ellipse whose principal axes align with the eigenvectors of M. This ellipse is then used to estimate the characteristics of the mean cell for an isotropic network (d.) and an oriented network (e.). Note: (i) Network description in (b.) does not, by any means, correspond to the network shown in (a.) and (ii) The plotted distributions in (d.) and (e.) are for illustrative purposes only and may not accurately reflect actual multicellular systems.

spanning all possible directions $(0 \le \theta < 2\pi)$ with all possible magnitudes $(0 < r < \infty)$. We can therefore define a distribution density function $\phi(X, r, t)$ to measure the number dn(X, r, t) of segment vectors with conformations lying within (r, r + dr) per unit conformation space per unit initial area a(0):

$$\phi(X, \mathbf{r}, t) := \frac{1}{a(0)} \frac{dn}{d\Omega} (X, \mathbf{r}, t)$$
 (2.2)

The nominal segment vector density c can then be expressed in terms of ϕ as:

$$c(X,t) = \int_{\Omega} \phi(X, \mathbf{r}, t) d\Omega$$
 (2.3)

where the integral is defined by any function (\blacksquare) of the random variable r (and its norm r = |r|) as:

$$\int_{\Omega} (\blacksquare) \ d\Omega = \int_{0}^{2\pi} \int_{0}^{\infty} (\blacksquare) \ r dr d\theta \tag{2.4}$$

Conveniently, c can also be related to the nominal concentration C(X,t) = N(X,t)/a(0) of cells in the network by invoking the average coordination number z. This number indeed measures the average number of connections per cell for a given population and hence relates the segment density c to the cell density c by c = (z/2)C, where a factor of 2 accounts for the fact that each connection is counted twice. For an asymptotically large population of confluent

cells away from the boundary, the average coordination z = 6. In the context of vertex models, z would represent the average number of sides of polygonal cells which can vary over time (Farhadifar et al., 2007). In such cases, z would be an additional state variable that would need to be solved but for simplicity, here we will assume that z remains a constant. In the remainder of this work, we will see that it is worthwhile to use a multiplicative split of the segment distribution density ϕ as:

$$\phi(X, \mathbf{r}, t) = c(X, t)p(X, \mathbf{r}, t) \tag{2.5}$$

where p(X, r, t) is the probability density function of the random variable r, that satisfies the classical requirement $\int_{\Omega} p(X, r, t) d\Omega = 1$. We emphasize again that the *conformation space*, Ω , which is the space over variable r, and its associated distributions (ϕ, p) represent the current state of the transient network at point X and hence drop the notation X hereafter. Also, the keyword *initial* used for defining area a(0) is important because it refers to the stressfree configuration at time t = 0 and not just any stress-free state as will become more clear in section 3.

2.3. Mean-field approximation

We will see in the subsequent sections how the above distribution densities (ϕ and p) can be used to describe the evolution of dynamic networks. But before that, one first needs to establish relationships between their expression and measurable quantities in the cellular assembly (notably the mean cell area A, mean circumference L, and nominal cell concentration C), which will eventually permit the evaluation of the elastic energy density from eqn. (2.1). For this, let us consider a known segment distribution density ϕ and attempt to determine C, A, and A. First, using eqn. (2.3) and the relation C = (z/2)C, the nominal cell concentration is found as:

$$C = \frac{2}{z} \int_{\Omega} \phi(\mathbf{r}) \, d\Omega \tag{2.6}$$

Let us now proceed to assess the mean cell area A and perimeter L by first expressing the covariance of the probability density p(r) using a second order, symmetric, positive definite tensor M defined as:

$$\mathbf{M} := \int_{\Omega} p(\mathbf{r}) \, \mathbf{r} \otimes \mathbf{r} \, d\Omega = \begin{pmatrix} \langle r_x^2 \rangle & \langle r_x r_y \rangle \\ \langle r_x r_y \rangle & \langle r_y^2 \rangle \end{pmatrix}$$
(2.7)

where \otimes denotes the dyadic product. Geometrically, the tensor M can be represented by a confidence ellipse \mathcal{E} whose semi-major axes' lengths and orientations describe the average shape of a cell as illustrated in Figs. Id. and Ie. Calculating the area and perimeter of this confidence ellipse (see Appendix A.I), the mean cell area A and perimeter A can be written as:

$$A = \pi \sqrt{|\mathbf{M}|}$$
 and $L = 2\pi \sqrt{\frac{\text{Tr}(\mathbf{M})}{2}}$ (2.8)

where operators $|\blacksquare|$ and $\text{Tr}(\blacksquare)$ denote the determinant and trace of a tensor (\blacksquare) respectively. We will demonstrate further in sections 3.1 and 4.1 how A and L are used to measure deformation in a cell network. For now, it is sufficient to understand that M, and hence (A, L), describe the current state of the population in the form of a composite or *mean cell*.

3. Continuum theory

For monolayers or tissues comprising a large number of cells, the network is expected to display an *emerging* behavior that transcends each individual stochastic event. At this macroscopic level, their mechanics is described by continuum models and characterized in terms of its *viscoelastic* and *growth* behavior. Biological growth is typically modeled as time-dependent plastic deformation in continuum mechanics. Mechanistically, topological transitions (cell intercalation, division, or apoptosis) can also be seen as time-dependent plastic rearrangements as these processes involve an "activation energy" leading to tissue's plastic behavior. This behavior, in a way, resembles yield-stress fluids (Coussot), [2014]; [Varchanis et al.], [2020]), with dynamic rearrangements occasionally driven by active mechanisms (which consume chemical energy). Tissue response is influenced not only by these inelastic processes but also significantly by changes in properties like preferred area A_R , contractility Γ , and junction tension Λ . This section aims to comprehensively outline the theoretical description of inelastic cellular mechanisms along with the role of material properties on complex tissue dynamics.

3.1. Kinematics

Consider a macroscopic solid tissue in its initial stress-free configuration defined by \mathcal{B}_0 . As this tissue deforms over time (due to growth, topological alterations, and external forces), it assumes a current deformed state represented by $\mathcal{B}(t)$. To characterize the deformation from \mathcal{B}_0 to $\mathcal{B}(t)$ (see Fig. 2), we introduce a Cartesian coordinate system with bases vectors $\{e_1, e_2\}$. In this system, the coordinate of a material point is noted X while it is denoted as a spatial point x = x(X, t) in the current deformed state. The function x (or motion) is here assumed to be continuous and differentiable over space and time. The deformation gradient tensor F(X, t) of a material point can then be introduced as the tangent mapping operator:

$$F(X,t) := \frac{\partial x}{\partial X} \tag{3.1}$$

The time derivative of this tensor may further be written in terms of the spatial velocity gradient ℓ so that:

$$\dot{F} = \ell F$$
 with $\ell = \frac{\partial \dot{x}}{\partial x}$ (3.2)

where the notation \dot{F} is used for the material time derivative. We now ask how the mean cell area, perimeter, and network distortion evolve as a function of this macroscopic deformation. To answer this, we draw upon the framework originally devised to model finite-strain elastoplasticity (Lee, 1969). According to this classical theory, when a body is elastically unloaded from its current state $\mathcal{B}(t)$ and all stresses are released, it does not revert to its *original* configuration \mathcal{B}_0 . Instead, due to irreversible deformations, it assumes a new, permanently altered stress-free (intermediate) state denoted as $\mathcal{B}_i(t)$, which itself may evolve over time. Alternatively, one could conceive of this state $\mathcal{B}_i(t)$ as if the body had undergone deformation from \mathcal{B}_0 solely through inelastic processes that do not result in any elastic stresses. This concept is more commonly recognized as multiplicative decomposition theory, wherein the complete deformation gradient F is expressed as:

$$F = F_e F_i \tag{3.3}$$

where F_e and F_i are, respectively, the elastic and inelastic components of the deformation gradient tensor. Consequently, the velocity gradient tensor ℓ is additively decomposed as $\ell = \ell_e + \ell_i$ where $\ell_e = \dot{F}_e F_e^{-1}$ and $\ell_i = F_e \dot{F}_i F_i^{-1} F_e^{-1}$. Therefore, we see that in order to construct an elasto-visco-plastic theory for confluent cell aggregates, one first needs to provide a proper definition of elastic deformation F_e , which in turn requires the description of reference or stressfree states: \mathcal{B}_0 and \mathcal{B}_i . Characterization of these states for biological materials has always been a topic of discussion (Hoger et al.) 2004; Du et al., 2018; Kupferman et al., 2020), primarily for two reasons: (1) Biological tissues are often residually stressed, signifying the presence of stored elastic energy even without external loads. (2) Minimum-energy configurations exhibit degeneracy, implying the existence of multiple stress-free arrangements. In addition to this, these states can evolve over time. In the next section, we will lay down the groundwork for our elasticity model (section Φ) by defining the stress-free configurations (Φ 0, Φ 1) within the framework of vertex models. To streamline our discussion, we divide stress-free states into two categories: one addressing the time-independent state and the other delving into time-dependent phenomena. The time-independent stress-free state serves as the *initial* configuration Φ 0 which is at equilibrium, while the *intermediate* configuration Φ 1 accommodates time-dependent inelastic processes and non-equilibrium response.

3.1.1. Initial stress-free configuration \mathcal{B}_0

In order to completely characterize our tissue state in \mathcal{B}_0 , we resort to the vertex model energy functional introduced in eqn. (2.1). It is customary (Bi et al., 2015) to omit the line tension term and express the energy functional \mathcal{E} as:

$$\mathcal{E} = N \left[\frac{K}{2} (A - A_R)^2 + \frac{\Gamma}{2} (L - L_R)^2 - \frac{\Lambda^2}{8\Gamma} \right]$$
 (3.4)

where $L_R = -\Lambda/(2\Gamma)$ is referred to as the preferred perimeter. Note that preferred area A_R and preferred perimeter L_R are not necessarily geometrically compatible and should be treated as two separate entities. Furthermore, for greater

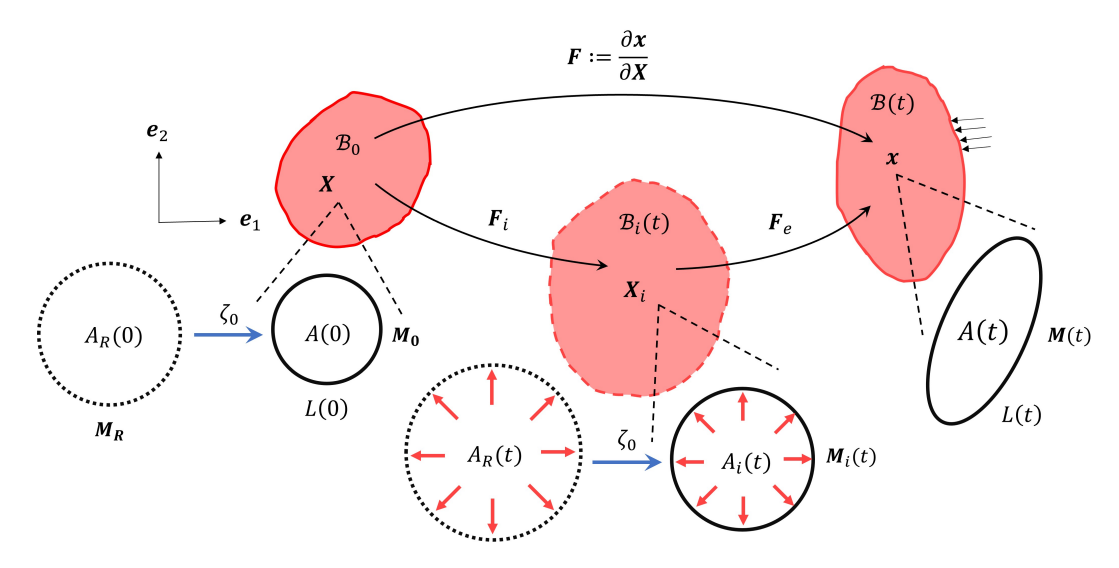


Figure 2: Mapping between initial, intermediate, and current configurations. Schematic of the underlying mean cell at arbitrary continuum points are shown as well.

utility, it is recommended to express the coefficients Γ and Λ in their non-dimensional forms: normalized contractility $\bar{\Gamma} = \Gamma/(KA_R)$ and normalized tension $\bar{\Lambda} = \Lambda/(KA_R^{3/2})$, respectively. By making this substitution in eqn. (3.4) and neglecting the term $\Lambda^2/(8\Gamma)$ (since it only shifts the total energy and does not contribute to the constitutive relations), we now rewrite our energy functional as:

$$\mathcal{E} = KNA_R^2 \left[\frac{1}{2} \left(\frac{A}{A_R} - 1 \right)^2 + \frac{\bar{\Gamma}p_p^2}{2} \left(\frac{L}{L_R} - 1 \right)^2 \right]$$
 (3.5)

where $p_p = L_R/\sqrt{A_R} = -\bar{\Lambda}/\left(2\bar{\Gamma}\right)$ is the preferred shape index. This shape index, initially introduced by Bi et al. (2015), sets up a competition between the preferred perimeter L_R and the preferred area A_R wherein the dominant term effectively sets the average shape of cells in the layer. More specifically, a high value of p_p is associated with cells that optimize their perimeter over their area and vice-versa for lower values. We can now evaluate the equilibrium state \mathcal{B}_0 by minimizing the energy in eqn. (3.5). Upon solving the minimization problem (Staple et al.) (2010), depending on p_p , the stable solution is either of the two following:

- (a.) The fluid state (when $A = A_R$ and $L = p_p \sqrt{A_R}$): This corresponds to the global minimum of \mathcal{E} and describe the configuration of cell network when cells tend to take their most optimum shape with preferred area A_R and preferred perimeter L_R . Cells in this configuration can form a realistic packing as long as they satisfy the constraint $p_p \geq 2\sqrt{\pi}$ (see Appendix A.2). Under this condition, the cell network is often referred to as *soft* or *fluid* because the network can not sustain any shear deformation due to its negligible shear resistance. It is also characterized by high fluctuation levels in the cell's motion as low energy barriers make the process of T1 transition effortless (Bi et al., [2015]).
- (b.) The solid-state (when $A < A_R$ and $L > p_p \sqrt{A_R}$): In this situation, the network is not in its absolute minimum energy state, but rather in a local minimum. The reason for this is because, unlike the fluid state, this state is geometrically incompatible since $p_p < 2\sqrt{\pi}$. As a consequence, when cells mechanically interact with each other to feasibly form a cohesive confluent tissue, they are locally deformed and induce residual stresses to restore *compatibility*. More specifically, cells are elastically compressed while their perimeter experiences tensile stresses (Tong et al., 2022) Staddon et al., 2023) that originate from a mismatch between L and L_R . The mean cell conformation in this case takes an area $A = \zeta_0 A_R$ that is *different* from its preferred area A_R by a factor of ζ_0 where this ζ_0 models residual elastic volumetric deformation. Note that since the compressive stresses within the cell are balanced by the tensile

stresses at cell boundaries, the overall aggregate in a macroscopic sense can be deemed stress-free.

As evident from the preceding discussion, confluent cell aggregates exhibit a *jamming transition* behavior that has been extensively investigated through vertex models (Bi et al., 2015) and continuum models (Kupferman et al., 2020). Staddon et al., 2023). Our focus here lies in characterizing both these phases within the statistical framework introduced in section 2.2 In a fluid state, cells reduce energy by expanding their contact area. This leads to their conformation as elongated polygons (as per-vertex models) or ellipses (in a coarse-grained context). Due to the random orientation of these ellipses, the network's average representation can be given by some isotropic covariance tensor $M_R = m_R I$, where I being the identity tensor, such that using eqn. (2.8) we can write initial preferred cell area $A_R(0) = \pi m_R$. Cells in the solid state, on the other hand, exist in the form of regular hexagons (as per-vertex models) and simply circular geometries (in a coarse-grained sense). Hence here also the network is isotropic represented by tensor $M_0 = m_0 I$ where the initial mean cell area A(0) is simply πm_0 . Recalling $A(0) = \zeta_0 A_R(0)$, we get $M_0 = \zeta_0 M_R$. Since we are interested in the solid-state tissue, which has finite bulks and shear modulus, M_0 describes the initial stress-free configuration \mathcal{B}_0 in our model. Also from the isotropic shape of the mean cell in this configuration, the corresponding perimeter L(0) is $2\sqrt{\pi A(0)}$. Assuming the initial cell count to be N(0), the energy $\mathcal{E}(0)$ in \mathcal{B}_0 can be found by simply substituting A = A(0), $A_R = A_R(0)$, L = L(0) and N = N(0) in eqn. (3.5) which results in:

$$\mathcal{E}(0) = e_0 \left[\frac{1}{2} (\zeta_0 - 1)^2 + \frac{\bar{\Gamma} p_p^2}{2} \left(\frac{2}{p_p} \sqrt{\pi \zeta_0} - 1 \right)^2 \right]$$
 (3.6)

where we introduce two scaling factors of energy and stress, respectively, given by

$$e_0 = KA_R(0)^2 N(0)$$
 and $\sigma_0 = KA_R(0)$ (3.7)

Note that ζ_0 in eqn. (3.6) is yet an unknown that needs to be determined. The procedure to obtain ζ_0 is outlined in section $\frac{1}{4}$ where we will show that ζ_0 is solely a function of material properties $\bar{\Gamma}$ and $\bar{\Lambda}$.

3.1.2. Intermediate stress-free configuration \mathcal{B}_i

In this section, we will introduce what cell-level mechanisms can operate in \mathcal{B}_i and how they can be translated to the macroscopic level to model growth mechanics in viscoelastic tissues. In this regard, we take a micro-mechanics-based approach consistent with vertex model rules to define our intermediate configuration \mathcal{B}_i . Before proceeding we would like to underline that while the rules for inelasticity have been motivated from vertex models, they are in general applicable to most confluent cell populations. Hence the proposed methodology can be extended to model a wide variety of systems.

The idea of the existence of an intermediate \mathcal{B}_i , in the context of biological materials, is usually applied to study growth within continuum mechanics. Consider a body initially stress-free, starts growing freely under some growth deformation tensor $F_g(X,t)$ (Lubarda and Hoger, [2002]; [Garikipati], [2009]; [Jones and Chapman], [2012]; [Goriely], [2017]; [Genet], [2019]). The resultant configuration $\mathcal{B}_i(t)$ at any time t with increased mass or volume or both, even though stress-free may or may not be physically compatible. Incompatibilities generally arise when the growth is inhomogenous ([Skalak et al.], [1996], [Jones and Chapman], [2012]). Elastic deformation F_e is then applied to restore compatibility. As a result of this, the current configuration $\mathcal{B}(t)$ becomes residually stressed.

In the absence of any inelastic activities, the tissue remains in equilibrium in \mathcal{B}_0 and the stored energy remains constant. However, if inelastic mechanisms are present, then the tissue comes out of equilibrium, and energy changes. This occurs when cells are able to change their preferred area $A_R(t)$ via expansion and/or division and number N(t) via cell divisions. Also since the tissue is growing stress-freely in $\mathcal{B}_i(t)$, its area $a_i(t)$ at any time t, is simply the area $A_i(t)$ of mean cell times the current number N(t) of cells in the population. The macroscopic inelastic volumetric deformation, given by Jacobian $J_i = |F_i|$, can then be expressed in terms of an *inelastic volumetric expansion ratio* ζ_i and a *cell number ratio* η such that:

$$\eta(t) = \frac{N(t)}{N(0)}, \qquad \zeta_i(t) = \frac{A_R(t)}{A_R(0)} = \frac{A_i(t)}{A(0)} \quad \text{and} \quad J_i(t) = \frac{a_i(t)}{a(0)} = \eta(t)\zeta_i(t)$$
(3.8)

Note that while writing the expression for ζ_i in eqn. (3.8), we have assumed that the residual elastic strain ζ_0 (i.e. the ratio of $A_i(t)$ to $A_R(t)$) remains unaffected from any deformation including inelastic deformations. At the same time, we assume no change in preferred shape index p_p . Based on this assumption the preferred cell perimeter $L_R(t)$ evolves with $\zeta_i(t)$ according to $L_R(t) = \sqrt{\zeta_i(t)}L_R(0)$. The implications of treating ζ_0 and p_p as material constants will be addressed further in sections 4 and 5 Now as is clear from eqn. (3.8), $J_i(t)$ arises from two processes: the inelastic deformation of individual cells (through the expansion term $\zeta_i(t)$) and the increase in cell number ratio $\eta(t)$ from cell division. These relations, therefore, provide a bridge between the mechanisms of proliferation and the deformation tensor I_R widely used in the growth literature.

The fundamental concept to grasp is that \mathcal{B}_i represents an intermediate stress-free configuration where cells experience growth, division, and intercalation. Since no external forces are applied, these processes unfold randomly, devoid of bias, thus maintaining isotropy within the network. Accordingly, the covariance tensor M_i in \mathcal{B}_i becomes $M_i(t) = \zeta_i(t)M_0$. Assuming that ζ_0 does not change during these processes and realizing that the network isotropy is not affected, energy in \mathcal{B}_i transforms to a time-dependent function $\mathcal{E}_i(t)$ given by:

$$\mathcal{E}_i(t) = \eta(t)\zeta_i^2(t)\mathcal{E}(0) \tag{3.9}$$

Equation (3.9) demonstrates how the energy of the tissue in \mathcal{B}_i changes due to cell growth and/or division. Despite the possibility of cells rearranging through passive T1 transitions in this configuration, these transitions do not alter the energy \mathcal{E}_i . This is simply because the mean cell conformation in an isotropic network remains unaffected by random intercalations.

It is important to reiterate that all discussions so far and in the remainder of the study pertaining to determining the macroscopic tissue state are centered around an arbitrary continuum point X. This state is influenced by the collective behavior of cells within a microscopic RVE-like region en-grained within that point. Our initial state \mathcal{B}_0 is a compatible state and no incompatibilities as a result of inelastic deformation F_i from \mathcal{B}_0 to \mathcal{B}_i arise at the scale of this RVE. However, since the macroscopic fields $(J_i(t), \zeta_i(t), \eta(t), A_i(t))$ are all, in general, functions of X where the argument X has been dropped, the notion of incompatibility emerging from non-uniform deformation fields remains valid. The tissue state, described by $\mathcal{B}_i(t)$, will now serve as a reference configuration for measuring elastic deformation.

3.1.3. Elastic deformation

When the tissue deforms due to applied external stress or through the cell proliferation process, which may be mechanically constrained, the network deforms into its current configuration $\mathcal{B}(t)$ represented by the covariance tensor M. We are now in a position to introduce the measure of elastic deformation with a strain-like quantity μ defined as:

$$\mu := \frac{M}{|M_i(t)|^{1/2}} = \frac{1}{\zeta_i} \frac{M}{|M_0|^{1/2}} = \frac{1}{\zeta_i} \frac{M}{m_0}$$
(3.10)

where $|\mathbf{M}_0|^{1/2} = m_0 = A(0)/\pi$ is the normalizing area that remains constant over time. In general, the tensor $\boldsymbol{\mu}$ is not isotropic and can be decomposed into an areal ζ_e and pure distortion (isochoric) component $\bar{\boldsymbol{\mu}}$ (verifying $|\bar{\boldsymbol{\mu}}| = 1$) as $\boldsymbol{\mu} = \zeta_e \bar{\boldsymbol{\mu}}$ where ζ_e defined as:

$$\zeta_e = \frac{A(t)}{A_i(t)} = |\mu|^{1/2} \tag{3.11}$$

is a dimensionless measure of the elastic expansion of the current mean cell area A(t) from its current reference state $A_i(t)$. With these definitions, μ satisfies the following properties: (a) it is represented by a tensor which is equal to the identity (I) when the tissue is in its intermediate stress-free configuration \mathcal{B}_i and (b) it varies due to both inelastic expansion ζ_i of cells and the application of pure elastic deformations.

At the macroscopic level, the volumetric deformation of the cell population is denoted by the Jacobian J = |F| of the total deformation gradient F. Following the multiplicative decomposition $F = F_e F_i$, J can also be split into a permanent (inelastic) contribution J_i (eqn. (3.8)) and an elastic contribution $J_e = |F_e|$ such that $J = J_e J_i$. By definition, $J_e = |F_e|$

can also be represented as the ratio of the current deformed area a(t) to the initial undeformed area a(0), resulting in:

$$J(t) = \frac{a(t)}{a(0)} = \frac{\zeta(t)N(t)A(0)}{N(0)A(0)} = \zeta(t)\eta(t)$$
(3.12)

where $\zeta = \zeta_e \zeta_i$ is simply a ratio of current mean cell area A(t) to its initial state A(0). Using this relation and eqn. (3.12), the elastic volumetric deformation $J_e(t)$ of the population is found to be equal to the average elastic deformation ζ_e experienced by each cell. This suggests that when a tissue behaves elastically, individual cells, on average, encounter the same deformation as the applied external deformation. However, when inelastic mechanisms start to operate, the deformation ζ_e felt by cells is different from the applied deformation J.

3.2. Time evolution of the elastic deformation

We will now see how the elastic deformation, as measured by μ , changes in response to external forces and cellular processes. For this, it is first worthwhile to derive an evolution equation for the distribution density ϕ and consequently, the probability density p, referred to as the Fokker-Planck equation. The derivation of the Fokker-Planck equation for a transient polymer network that can stochastically gain and lose segments over time has been discussed in detail in previous work (Vernerey et al.) [2017). For this reason, we defer derivations to the appendix (see Appendix B.1). Again consider our conformation space Ω . Since this region is defined for each material point X, no heterogeneities in terms of macroscopic quantities exist within Ω . In other words, it is assumed that the deformation gradient F(X,t) is translated uniformly throughout Ω . As a result, the elastic motion of existing segments (between the time they are created and deleted) deform affinely with macroscopic deformation, and we can write $\dot{r} = \ell r$ where $\ell = \dot{r}F^{-1}$ is the macroscopic velocity gradient. In addition, if the rates of segment creation and loss are represented by functions ξ_c and ξ_l , respectively, the time evolution of $\phi(r,t)$ for our compressible cellular network is expressed by:

$$\dot{\phi} = -\boldsymbol{\ell} : \left(\frac{\partial \phi}{\partial \boldsymbol{r}} \otimes \boldsymbol{r}\right) - \text{Tr}(\boldsymbol{\ell}) \phi + \xi_c(\boldsymbol{r}) - \xi_l(\boldsymbol{r})$$
(3.13)

where the first two terms arise from the convection of existing segments with the velocity gradient ℓ while the last two terms exemplify topological changes within the network. The vertex model extensively considers three kinds of topological transformations (Staple et al., 2010): cell intercalation (also known as T1 transition), cell division, and cell apoptosis (also known as T2 transition). We note that all three are characterized as **irreversible kinetic events** and can depend on a number of biomechanical and biochemical factors. To name a few such as cell density, cell shape, stress, and nutrient availability. These transitions, along with cell growth, are the primary contributors to tissue growth and morphogenesis. To see how they affect cell number ratio η and cell state μ , we carry out two operations. First, using $\phi = (z/2)Cp$ and eqn. (2.6), the differential equation (3.13) can be used to obtain the following evolution for η (see Appendix B.2) as:

$$\dot{\eta} = \frac{2}{zC(0)} \int_{\Omega} \dot{\phi} \, d\Omega = \frac{2}{zC(0)} \left(\Xi_c - \Xi_l \right) \tag{3.14}$$

where C(0) = 1/A(0) is the initial nominal cell density and the overall rates of creation and depletion of segment vectors are written respectively,

$$\Xi_c = \int_{\Omega} \xi_c d\Omega$$
 and $\Xi_l = \int_{\Omega} \xi_l d\Omega$ (3.15)

Second, combining eqns. (3.13) and (3.14), we can now write the evolution equation for the probability density $p(\mathbf{r}, t)$

$$\dot{p} = -\boldsymbol{\ell} : \left(\frac{\partial}{\partial \boldsymbol{r}} \otimes (p\boldsymbol{r})\right) + 2\frac{\xi_c - p\Xi_c}{z\eta C(0)} - 2\frac{\xi_l - p\Xi_l}{z\eta C(0)}$$
(3.16)

which is our Fokker-Planck equation as derived in Appendix B.3. Taking the covariance of this equation quickly yields an evolution equation for the covariance tensor M as:

$$\dot{\mathbf{M}} = \int_{\Omega} \dot{p} \, \mathbf{r} \otimes \mathbf{r} \, d\Omega = \ell \mathbf{M} + \mathbf{M} \ell^{T} + 2 \int_{\Omega} \left(\frac{\xi_{c} - p\Xi_{c}}{z \eta C(0)} \right) \mathbf{r} \otimes \mathbf{r} \, d\Omega - 2 \int_{\Omega} \left(\frac{\xi_{l} - p\Xi_{l}}{z \eta C(0)} \right) \mathbf{r} \otimes \mathbf{r} \, d\Omega$$
(3.17)

Note that this equation can therefore be used to follow the evolution in cell area and perimeter via relations (2.8). To further simplify the notation, one can invoke the definition of the Lie derivative of a tensor (here M) convected by the velocity gradient ℓ , written in the form:

$$\mathcal{L}(\mathbf{M}) = \dot{\mathbf{M}} - \ell \mathbf{M} - \mathbf{M} \ell^{T} \tag{3.18}$$

The evolution of M can now be re-written in the simpler format:

$$\mathscr{L}(\mathbf{M}) = \frac{2}{z\eta C(0)} \left[\int_{\Omega} (\xi_c - p\Xi_c) \, \mathbf{r} \otimes \mathbf{r} \, d\Omega - \int_{\Omega} (\xi_l - p\Xi_l) \, \mathbf{r} \otimes \mathbf{r} \, d\Omega \right]$$
(3.19)

The convective rate of elastic deformation can now be derived using the relation $C(0)m(0) = 1/\pi$ and eqns. (3.19), (3.10). This rate is represented by the tensor:

$$\mathscr{L}(\boldsymbol{\mu}) = -\frac{\dot{\zeta}_{l}}{\zeta_{l}}\boldsymbol{\mu} - \left(\frac{2\pi}{z}\right)\frac{1}{J_{l}}\left[\int_{\Omega} (\xi_{l} - p\Xi_{l})\,\boldsymbol{r}\otimes\boldsymbol{r}\,d\Omega - \int_{\Omega} (\xi_{c} - p\Xi_{c})\,\boldsymbol{r}\otimes\boldsymbol{r}\,d\Omega\right]$$
(3.20)

In the next few sections, we concentrate on articulating different inelastic cellular processes associated with T1 transitions (denoted by a subscript D), cell division (denoted by a subscript D), and cell growth (denoted by subscript G). More specifically we will look into deriving the explicit forms of flow rates due to inelastic deformations pertaining to T1 transitions (d_T), cell divisions (d_D), and cell growth (d_G). The complete theoretical model can then be captured by the flow rule:

$$\mathcal{L}(\mu) = \dot{\mu} - \ell \mu - \mu \ell^T = -d_T - d_D - d_G \quad \text{and} \quad \dot{\eta} = \dot{\eta}_T + \dot{\eta}_D + \dot{\eta}_G$$
 (3.21)

where $\dot{\eta}_T$, $\dot{\eta}_D$, $\dot{\eta}_G$ are the changes in cell number ratio due to T1 transition, cell division, and cell growth respectively. To connect the above expression with classical models, let us consider the purely elastic situation where growth, divisions, and intercalations do not occur. In this case, eqn. (3.21) becomes:

$$\mathcal{L}(\boldsymbol{\mu}) = 0 \qquad \text{and} \qquad \dot{\eta} = 0 \tag{3.22}$$

The solution of this equation is $\mu = FF^T$, i.e. the elastic tensor degenerates to the classical left Cauchy-green deformation tensor b. In the case where inelastic processes take place, the elastic deformation μ may change due to topological transitions and/or cell expansion. These mechanisms are discussed in detail in section 5. For the time being, we concentrate on the macroscopic elastic response of the cell aggregate.

3.3. Thermodynamic formalism

In this section, we will develop a general framework for deriving the constitutive relations for a growing viscoelastic solid. We start by postulating the existence of a Helmholtz free energy function ψ defined per unit mass. This potential, in general, is a function of the elastic deformation tensor μ and a set of history-dependent internal state variables (ISVs) $\chi = \{\chi_1, \chi_2, \chi_3, ..., \chi_m\}$ that define the thermodynamic state of the material at any time t. Mathematically we write:

$$\psi = \psi(\mu, \chi) \tag{3.23}$$

where the elements of χ are, in general, second-order tensors characterizing the inelastic mechanisms that include growth, remodeling, and dissipative rearrangements inside our material. Next, we employ the Clausius-Duhem form of the second law of thermodynamics, which states that internal dissipation \mathcal{D} (per unit current volume) for an open system (that can change mass) under iso-thermal (constant temperature) and adiabatic (no heat transfer) conditions should satisfy (Huang et al., 2021):

$$\mathscr{D} = \boldsymbol{\sigma} : \boldsymbol{\ell} - \rho \dot{\boldsymbol{\psi}} \ge 0 \tag{3.24}$$

where σ is the Cauchy stress tensor, ρ is the mass density defined per unit current volume and $\dot{\psi}$ is the material time derivative of ψ . The first term $\sigma: \ell$ is the rate of work done by internal forces per unit current volume and

is often represented by W_{int} . For systems that are growing as a result of the change in mass, it is more useful to introduce another measure of Helmholtz free-energy density ψ_i defined per-unit volume in the intermediate stress-free configuration:

$$\psi_i = \rho_i \psi$$
 where $\rho_i = J_e \rho$ (3.25)

is the mass density defined per unit volume in intermediate stress-free configuration \mathcal{B}_i . Most continuum growth theories assume that ψ_i is only a function of elastic deformation F_e and is independent of any growth-related variables. Here, we consider the general case where ψ_i , not only depends on μ , but also on the ISVs χ . Hence:

$$\psi_i = \psi_i(\mu, \chi) \tag{3.26}$$

As per the multiplicative decomposition theory $F = F_e F_i$, mass growth only takes place between \mathcal{B}_0 and \mathcal{B}_i . In other words, the mass of the system in the current configuration \mathcal{B} is the same as the mass in \mathcal{B}_i . Using this condition we can get the required relation (3.25) between ρ and ρ_i . Now substituting for ψ and ρ from eqn. (3.25) in eqn. (3.24), we can rewrite our Clausius-Duhem inequality as:

$$\mathscr{D} = \boldsymbol{\sigma} : \boldsymbol{\ell} - \frac{1}{J_e} \dot{\psi}_i + \frac{1}{J_e} \frac{\dot{\rho}_i}{\rho_i} \psi_i \ge 0 \tag{3.27}$$

where $\dot{\psi}_i$ from eqn. (3.26) can be expressed using chain rule as:

$$\dot{\psi}_i = \frac{\partial \psi_i}{\partial \mu} : \dot{\mu} + \sum_{a=1}^m \frac{\partial \psi_i}{\partial \chi_a} : \dot{\chi}_a$$
 (3.28)

The first term includes partial derivatives with respect to invariants I_1 , I_2 , I_3 of tensor μ while the second term accounts for the change in ψ_i due to inelastic rates $\dot{\chi}_a$. We will now use this Clausius-Duhem inequality (3.27) and eqn. (3.28) to first derive an expression for Cauchy stress tensor σ in section 4 and then later to investigate the growth and viscoelasticity behavior of confluent cell monolayers in section 5.

4. Elasticity model

In this section, we focus on the elastic behavior of tissue where cells do not grow, divide, or intercalate and therefore $\mathcal{L}(\mu) = 0$ and $\dot{\eta} = 0$. For our purposes, we use the vertex model energy functional (3.5) and vertex model-based stress-free states (sections 3.1.1 and 3.1.2) to derive our material model.

4.1. Network stress

Having quantified all stress-free configurations \mathcal{B}_0 and \mathcal{B}_i as well as the elastic deformation, we can now summarize our current mean cell area A(t) and perimeter L(t) in terms of continuum variables (see Appendix B.4):

$$\frac{A}{A_R} = \zeta_0 \zeta_e \quad \text{and} \quad \frac{L}{L_R} = \frac{2}{p_p} \sqrt{\frac{\pi \zeta_0 I_1}{2}}$$
 (4.1)

where $\zeta_e = J_e = \sqrt{I_3} = \sqrt{|\mu|}$ and $I_1 = \text{Tr}(\mu)$ are the invariants of the elastic tensor μ . Using eqns. (3.5), (3.7), (3.8), and (4.1) the energy $\mathcal{E}(t)$ of tissue in current configuration $\mathcal{B}(t)$ can be expressed in terms of dimensionless quantities I_1, I_3, η, ζ_i as:

$$\mathcal{E}(I_1, I_3; \eta, \zeta_i) = e_0 \eta \zeta_i^2 \left[\frac{1}{2} (\zeta_0 \zeta_e - 1)^2 + \frac{\bar{\Gamma} p_p^2}{2} \left(\frac{2}{p_p} \sqrt{\frac{\pi \zeta_0 I_1}{2}} - 1 \right)^2 \right]$$
(4.2)

where note that we have split the arguments to distinguish between elastic deformation measures (I_1, I_3) and *ISVs* (η, ζ_i) . The Helmholtz -free energy density ψ_i defined as $\psi_i = \mathcal{E}/a_i$ can now finally be written as:

$$\psi_i(I_1, I_3; \zeta_i) = \sigma_0 \zeta_i \left[\frac{1}{2\zeta_0} \left(\zeta_0 \sqrt{I_3} - 1 \right)^2 + a \left(b \sqrt{I_1} - 1 \right)^2 \right]$$
(4.3)

where the non-dimensional material coefficients a and b are, respectively, given by:

$$a = \frac{\bar{\Gamma}p_p^2}{2\zeta_0} \quad \text{and} \quad b = \frac{\sqrt{2\pi\zeta_0}}{p_p} \tag{4.4}$$

One can now use this frame-invariant definition of Helmholtz free energy density ψ_i (4.3) and Clausius-Duhem inequality (3.27) to obtain the Cauchy stress tensor σ , which, takes the form (see Appendix C) of a hyper-elastic material:

$$\sigma = \frac{2}{J_e} \frac{\partial \psi_i}{\partial \mu} \mu = \frac{2}{J_e} \left[\frac{\partial \psi_i}{\partial I_1} \mu + \frac{\partial \psi_i}{\partial I_3} I_3 I \right]$$
(4.5)

Substituting ψ_i from eqn. (4.3) in the above results in our constitutive relation:

$$\sigma(I_1, I_3; \zeta_i) = 2\sigma_0 \zeta_i \left[\frac{1}{2} \left(\zeta_0 \sqrt{I_3} - 1 \right) \mathbf{I} + ab \left(b - \frac{1}{\sqrt{I_1}} \right) \bar{\boldsymbol{\mu}} \right]$$

$$\tag{4.6}$$

where recall that $\bar{\mu} = \mu/J_e$ is the isochoric part of μ . The result in eqn. (4.6) is in a way similar to that of Ishihara et al. (2017) where the first term models isotropic pressure due to area elasticity and the second term represents cell-shape dependent stress due to junction tensions. The differences, though, lie in the inclusion of a state variable ζ_i , representing inelastic cell expansion, and an additional material property ζ_0 , characterizing the volumetric residual elastic strain in solid-state tissues. Also, the current model is valid only when adhesion dominates i.e. $\bar{\Lambda} < 0$ or $p_p > 0$, which explains the negative contribution to stress from μ in eqn. (4.6). This range of material property values ($p_p > 0$) is comprehensive enough and encompasses the entire spectrum of solid-state tissues except for a small range where contractility dominates $\bar{\Lambda} > \approx 0$ before the response of tissue becomes inconsistent with observations as per the vertex models (Bi et al.) (2015).

The previously unknown residual deformation ζ_0 can now be determined by solving for $\sigma=0$ when $\mu=I$ signifying stress-free tissue. The results for ζ_0 are plotted in Fig. 3 which shows that the model parameters $\bar{\Gamma}$ and $\bar{\Lambda}$ greatly influence the values of ζ_0 . For instance, one observes that the cell's internal pressure increases (i.e. ζ_0 decreases) with the cortex contractility $\bar{\Gamma}$ for a constant normalized tension $\bar{\Lambda}$. For the remainder of this study, we only consider confluent tissues in their solid state, i.e. $\zeta_0 < 1$, and $p_p < 2\sqrt{\pi} (= 3.545)$. Also since ζ_0 depends only on material properties $\bar{\Gamma}$, $\bar{\Lambda}$, it remains constant as long as $\bar{\Gamma}$ and $\bar{\Lambda}$ do not change.

4.2. Elastic response of cell network

To illustrate the prediction of the elastic model, we examine the elastic response of epithelial tissue under uni-axial stretch and more specifically investigate the impact of the material properties $\bar{\Gamma}$ and $\bar{\Lambda}$ on its Young's modulus Y and Poisson's ratio ν . Indeed, while these parameters are usually defined for linearized elasticity, they can be extracted for a non-linear model as follows:

$$Y = \frac{\sigma_1}{\lambda_1 - 1} \qquad \text{and} \qquad v = \frac{-log(\lambda_2)}{log(\lambda_1)}$$
(4.7)

where σ_1 is the applied longitudinal Cauchy stress component and $F = diag[\lambda_1, \lambda_2]$ is the resultant deformation gradient. The numeric values of unknowns λ_1 and λ_2 are obtained by substituting $\mu = FF^T$ in eqn. 4.6 and then numerically solving for $\sigma(\lambda_1, \lambda_2) = diag[\sigma_1, 0]$. Using these relations, Fig. 4 depicts how the tissue stiffness Y and Poisson's ratio ν depend on cellular scale properties $\bar{\Gamma}$, $\bar{\Lambda}$. These results indicate that the tissue properties change in a nontrivial manner with cell junction tension and contractility. One can generally identify two main regions in the $\{\bar{\Gamma}, \bar{\Lambda}\}$ space. Near the jamming transition region $(p_p = 2\sqrt{\pi})$, the tissue behaves more like an incompressible fluid $\nu \approx 1$ with vanishing stiffness $Y \approx 0$. Upon increasing $\bar{\Gamma}$ and $\bar{\Lambda}$ the tissue becomes stiffer as can be seen in region 1 in plot 4. The model predicts a constantly decreasing Poisson's ratio with increasing cell tension and contractility within region 1 in plot 4. Further increase in $\bar{\Gamma}$ and $\bar{\Lambda}$ pushes the tissue to a new state (region 2, plot 4a.), where the stiffness reaches a maximum before dropping fairly quickly (but remaining positive). This region (see plot 4b.) is also characterized by a negative Poisson's ratio ν . In a qualitative sense, these predictions are in good agreement with

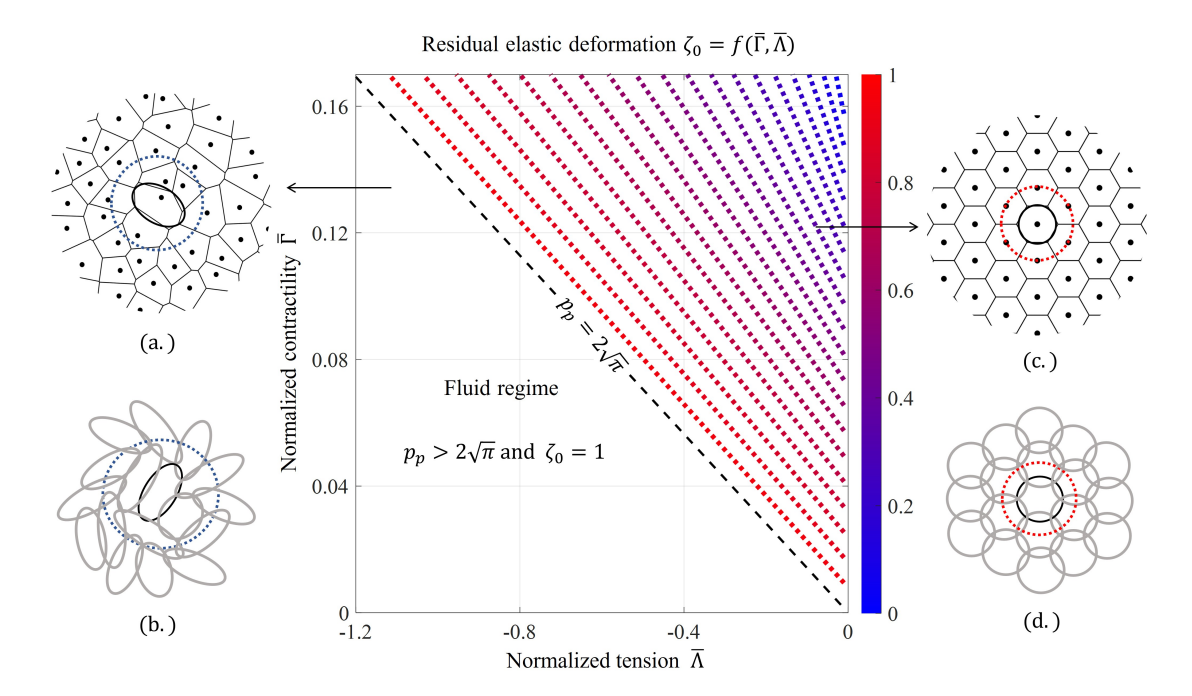


Figure 3: Continuum interpretation of vertex model equilibrium states in different phases: Left: A fluid regime where cells take *elongated* shapes and are fully relaxed and the cell packing is highly irregular and degenerate. Statistics of the network will still correspond to some isotropic tensor shown by confidence ellipse (dashed blue in (a.) and (b.)) with area and perimeter equal to $A_R(0)$ and $p_P \sqrt{A_R(0)}$ respectively. Right: The cell geometry in the solid-state condition corresponds to a regular n-sided polygon in vertex models. On a network level, this equilibrium state has regular hexagonal packing (c.) which translates to an array of *roundish* cells in our continuum formulation (d.) as illustrated by the confidence ellipse (dashed red) with area and perimeter as A(0) and $2\pi \sqrt{A(0)}$ respectively. Center: The magnitude of compression in cells ($\zeta_0 = A(0)/A_R(0)$) in a *solid* tissue is plotted as a function of material properties ($\bar{\Gamma}$, $\bar{\Lambda}$).

vertex model simulations conducted by Merzouki et al. (2016) using the same loading parameters. Again recall that our model is invalid for cases where $\bar{\Lambda} > 0$ (or $p_p < 0$). The results for this region, therefore, can not be compared with Merzouki et al. (2016).

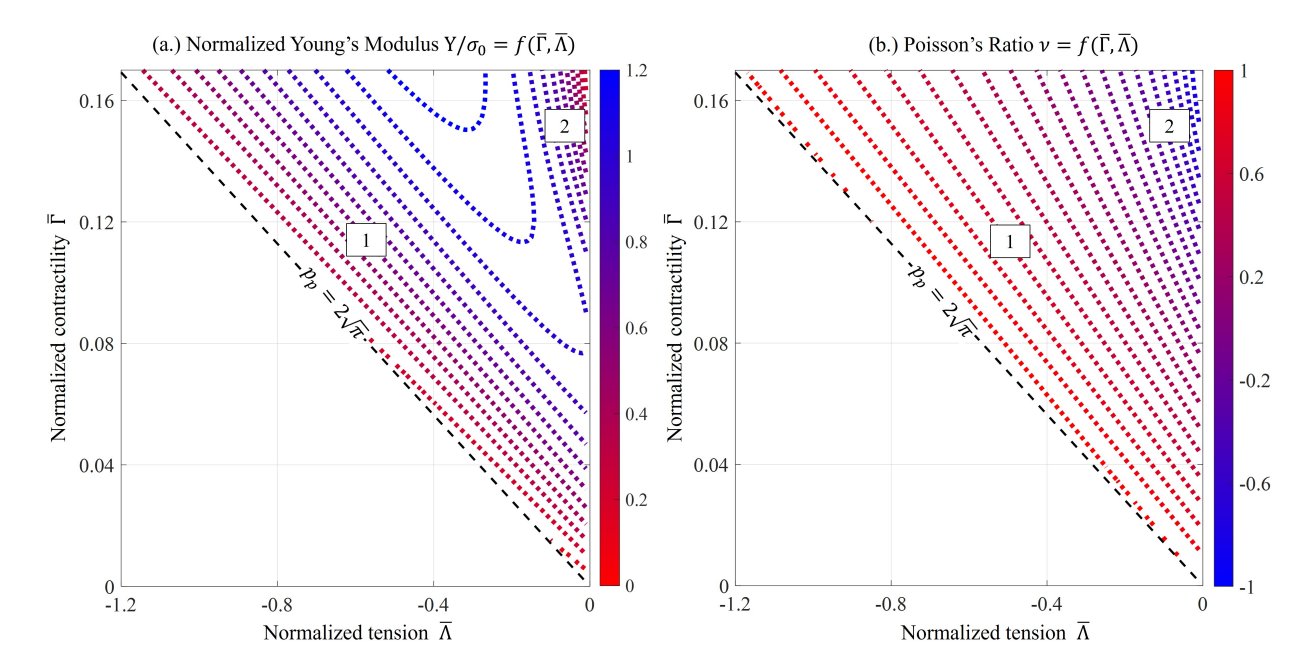


Figure 4: The tissue's stress scaling factor is $\sigma_0 = \pi$ and is loaded under un-axial tension with $\sigma_1 = 0.0738\sigma_0$ and $\sigma_2 = 0$. The material parameters $\bar{\Gamma}$ and $\bar{\Lambda}$ are selected to keep the tissue in the elastic regime, and iso-contours of Young's modulus (a.) and Poisson's ratio (b.) are plotted accordingly. **Note**: The values presented here should not be considered elasticity constants for biological tissues. This is due to the non-linear hyper-elastic nature of biological materials, which results in the dependence of their elastic properties on deformations.

5. Inelasticity model

With the tissue elasticity fully defined, we now turn to inelastic processes, starting with T1 transitions followed by division and proliferation. While the constitutive laws derived for topological rearrangements eventually align with (Ishihara et al., 2017), we accentuate that the current framework, in comparison to (Ishihara et al., 2017), is equipped to differentiate between different rearrangements and their macroscopic effects. This is achieved by employing a novel approach that links the flow rates to their microscopic descriptions. Subsequently, we will also thoroughly discuss the mechanics of cell proliferation, a topic that is often overlooked in growth as well as coarse-grained continuum theories.

5.1. T1 Transition

A T1 transition is a type of topological rearrangement where cells swap neighbors. A variety of such transitions may occur (such as rosette formations (Fletcher et al.) (2014)), but for convenience, we here limit ourselves to the case when swapping involves a bond exchange between cells. Also, for the remainder of this study, we confine ourselves to the case of passive T1 transitions.

Rate of passive T1 transition: T1 transitions modify the local topology of cellular networks as shown in Fig. 5 without affecting the total number of segment vectors. Following ideas from the experimental work of Marmottant et al. (2009) and vertex model studies, we postulate that these transitions occur stochastically at a rate k_T , which may itself be affected by the cell state. Thus, one may write general evolution laws for ξ_c and ξ_l (first appearing in eqn. (3.13)) in the following form:

$$\xi_c(\mathbf{r}) = k_T \frac{z}{2} C p^*(\mathbf{r})$$
 and $\xi_l = k_T \frac{z}{2} C p(\mathbf{r})$ (5.1)

These expressions ensure that the rates at which segment vectors are created and deleted are the same and equal to the base rate $k_T(z/2)C$ (Fig. 5(b.) and 5(d.)). Furthermore, the probability density functions (pdf's) p^* and p characterize

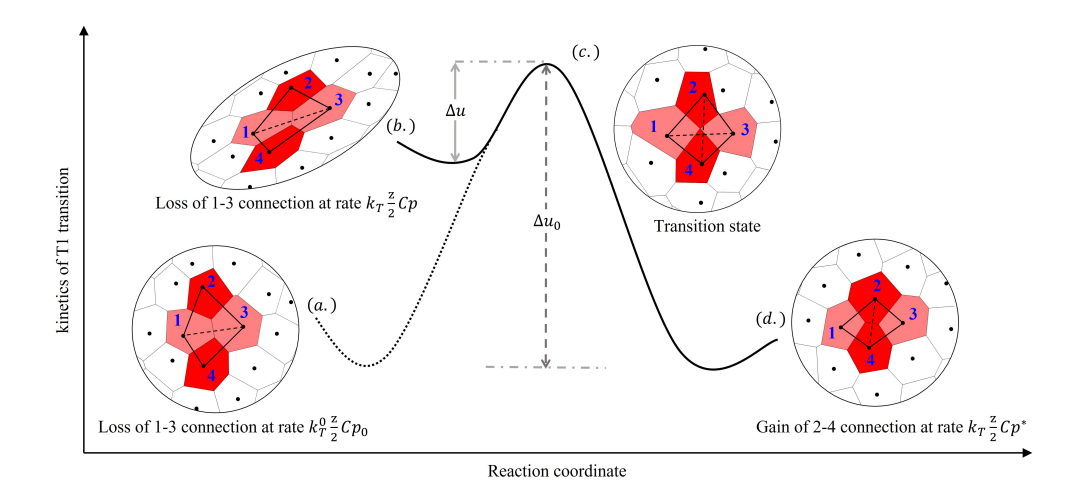


Figure 5: TNT illustration of cell intercalation: T1 transitions from the ground state (a.) with probability density p_0 to state (d.) with probability density p^* via transition state (c.) are fluctuation-induced. Once sufficiently deformed, they readily rearrange and go from the current deformed state (b.) with probability density p to (d.) in which case we refer to them as stress-induced rearrangements. The source of stress could be passive (external) as shown here or active (internal).

the conformations at which those segments are created and deleted respectively. Using the properties of pdf's, the overall rates of creation and loss are directly obtained from eqn. (3.15) as $\Xi_c = k_T(z/2)C$ and $\Xi_l = k_T(z/2)C$. This confirms that the overall change in cell number does not change during a T1 transition, i.e.:

$$\dot{\eta}_T = \frac{2}{zC(0)} (\Xi_c - \Xi_l) = 0 \tag{5.2}$$

Depending on the state of the tissue, T1 transitions may occur at constant rates (more notably for fluid-like tissues) or maybe energy activated (for solid-like tissues). Following the transition state theory (Eyring, 1936), we postulate the existence of activation energy Δu (see Fig. 5) such that the rate of T1 transitions, given by k_T , follows an Arrhenius-type relation (Bi et al., 2014):

$$k_T = \mathscr{A} \exp\left[-\frac{\Delta u}{\epsilon}\right] \tag{5.3}$$

where \mathscr{A} is the inherent attempt frequency of junction rearrangement and ϵ is the energy that can be used by cells to explore their other possible equilibrium configurations by overcoming any energy obstacles. This energy could be provided either by active mechanisms (i.e. ATP driven) or by passive mechanisms (i.e. elastic energy stored in junctions due to external deformation). Thus, in the case of a fluid tissue, the energy barrier is low and T1 transitions occur in a permanent fashion, while in a solid tissue, cells do not intercalate until they are been sufficiently deformed (Marmottant et al., 2009). Following (Butler et al., 2009), the deformation energy (Δu) is here expressed in terms of the deviation of a cell from circularity. This can be measured by a dimensionless quantity $\chi = \sqrt{\bar{I}_1/2}$ where \bar{I}_1 is the first invariant of $\bar{\mu}$ such that $\chi = 1$ for a circular geometry. We here postulate that the energy Δu is a quadratic function of χ in the form:

$$\Delta u = \Delta u_0 - \frac{\varrho r}{2} (\chi - \chi_c)^2 \quad \text{if} \quad \chi > \chi_c \tag{5.4}$$

where Δu_0 is the ground-state energy barrier, ϱ_T is a stiffness-like parameter and χ_c is the critical value of cell distortion that sets the yield criteria. Below the yield, we have $\Delta u = \Delta u_0$ and hence cells rearrange with the rate k_T^0 given by $k_T^0 = \mathcal{A} \exp(\Delta u_0/\epsilon)$. This rate is often called the fluctuation-induced rearrangement rate because the energy available for overcoming the barrier comes from random junction fluctuations. The final rate of the T1 transitions, which now are stress-induced, can be written as:

$$k_T(\chi) = k_T^0 \exp\left[\frac{\varrho_T}{2\epsilon} (\chi - \chi_c)^2\right] \quad \text{if} \quad \chi > \chi_c$$
 (5.5)

and $k_T = k_T^0$ otherwise. Thus, when $\chi < \chi_c$, cells are in a jammed state, while as χ increases above its critical value of χ_c , cell rearrangement occurs at an increasing rate.

Inelastic deformation rate from T1 transitions We are now in a position to express the rate of inelastic deformation that arises from T1 transitions. For this, we substitute expressions for ξ_c , ξ_l , Ξ_c , Ξ_l into eqn. (3.20) in the absence of cell proliferation (i.e. $\dot{\xi}_i = 0$) and quickly obtain the following expressions:

$$d_T = k_T(\chi) (\mu - \mu_T) \qquad \text{where} \qquad \mu_T = \frac{1}{m_0} \frac{1}{\zeta_i} \int_{\Omega} p^* \mathbf{r} \otimes \mathbf{r} d\Omega$$
 (5.6)

is the normalized covariance of the segment conformation following a T1 transition. Generally, a T1 transition occurs such that it allows distorted cells to recover a more isotropic state. This isotropic state corresponds to the isotropic tensor $\mu_T = \mu_T I$, with I the two-dimensional identity tensor and μ_T a (still) unknown quantity. Using the fact that T1 transitions do not produce any permanent changes in volume, we demonstrate in Appendix D.1 that the tensor μ_T must verify the relation $\text{Tr}(\mu_T \mu^{-1}) = 2$. Using this relation, we find that $\mu_T = 2/\text{Tr}(\mu^{-1})$, and thus the rate of plastic flow becomes:

$$d_T = k_T(\chi) \left(\mu - 2 \frac{I}{\text{Tr}(\mu^{-1})} \right)$$
(5.7)

Notice that d_T remains non-zero i.e. cells continue to intercalate until they fully recover the isotropic state given by $\mu = 2/\operatorname{Tr}(\mu^{-1})I$. As shown in Appendix D.1 this expression (5.7) enforces that the inelastic deformation from the T1 transition is purely deviatoric. Therefore, when the tensor μ is isotropic, the stress (eqn. (4.6)) state is hydrostatic and T1 transitions do not influence the macroscopic configuration of the tissue (since in such a case $d_T = 0$). The stress state only changes if cells are deformed anisotropically, i.e. $\bar{\mu} \neq I$.

Dissipation due to passive T1 transitions: As mentioned earlier, T1 transitions can result from active cellular processes, in which case they can generate stresses and drive tissue deformation such as in convergent extension (Tetley and Mao | 2018; Popović et al. | 2017; Duclut et al. | 2022). Conversely, intercalation in response due to external deformation can be a purely passive process. In the latter case, T1 transitions contribute to the relaxation of elastic stresses (Ishihara et al. | 2017) and should be thermodynamically dissipative. To determine the thermodynamic admissibility of constitutive equation d_T (5.7) for passive T1 transitions we again refer to the Clausius-Duhem inequality (3.27) to derive an equation for dissipation \mathcal{D}_T as (see Appendix D.2):

$$\mathscr{D}_T = \frac{1}{J_e} \frac{\partial \psi_i}{\partial I_1} k_T \operatorname{Tr} \left(\boldsymbol{\mu} - \frac{2}{\operatorname{Tr}(\boldsymbol{\mu}^{-1})} \boldsymbol{I} \right) = \frac{1}{J_e} \frac{\partial \psi_i}{\partial I_1} \operatorname{Tr}(\boldsymbol{d}_T)$$
(5.8)

which should satisfy $\mathcal{D}_T \geq 0$. It can be shown that the term $k_T \operatorname{Tr}(\mu - 2/\operatorname{Tr}(\mu)^{-1}I)$, which is same as $\operatorname{Tr}(d_T)$, is always non-negative for any general case of μ . Furthermore, for \mathcal{D}_T to remain greater than or equal to zero at all times, the derivative elastic energy density ψ_i with respect to the first invariant of μ tensor should also satisfy $\partial \psi_i / \partial I_1 \geq 0$. This condition yields an interesting constraint on the extent of elastic deformation where I_1 must always be greater than or equal to $p_p^2/(2\pi\zeta_0)$. We hypothesize that this limit, which completely depends on material parameters $\bar{\Gamma}$ and $\bar{\Lambda}$ ensures tissue integrity due to the interplay between the mechanics of adhesion $(\bar{\Lambda})$ and contractility $(\bar{\Gamma})$. The physical meaning of I_1 can be translated as inter-cellular distance ratio $r(t)^2/r_i(t)^2$ where r(t) is the current average value of segment length (same as average inter-cellular distance) and $r_i(t)$ is its reference value in the stress-free state $\mathcal{B}_i(t)$. Attempting to reduce this r with respect to r_i via elastic deformation, below a certain limit, will violate the stress equilibrium between the tensile residual stresses in junctions and the residual compressive stresses in the cell bulk. This condition is therefore an outcome of using the particular energy functional (3.5) as used in vertex models and related continuum models (5taddon et al., 2023) and which is built upon the mechanics of junction tension $(\bar{\Lambda})$ and cell contractility $\bar{\Gamma}$. Overall the equation. (5.8) ensures that passive T1 transitions result in positive entropy production as long as tissue compatibility is maintained.

5.1.1. Illustrations

Let us now illustrate the model's prediction in two simple cases: (a.) the stress relaxation and (b.) the shear rheology of confluent tissues. Results are then qualitatively compared to those obtained from vertex simulations and other

related studies.

(a.) Passive stress relaxation. Our first example examines the role of cell intercalation on the long-term stress-relaxation of confluent tissues. Ishihara et al. (2017) demonstrated the passive stress relaxation due to T1 transitions in an epithelial tissue that was loaded under bi-axial isochoric deformation. For our illustration, we will perform a uni-axial-stretch test in which the tissue is free to deform along the transverse direction. Consider a homogeneous domain whose motion is recorded in a 2D Cartesian coordinate system with unit basis vectors $\{e_1, e_2\}$ (Fig. [6]a.). In this frame, the sample is subjected to a spatially uniform uni-axial stretch ratio λ_1 along e_1 . The deformation is applied at a constant true strain rate ℓ_1 such that the velocity gradient becomes

$$\ell = diag[\ell_1, \ell_2]$$
 where $\ell_1 = \dot{\lambda}_1/\lambda_1$ and $\ell_2 = \dot{\lambda}_2/\lambda_2$

Considering that the sample is free in the lateral direction (i.e. the Cauchy stress component σ_2 vanishes), the resulting transverse strain rate, ℓ_2 (and associated stretch ratio λ_2) remains undetermined and needs to be solved for. In these conditions, the evolution of the elastic tensor $\mu = diag[\mu_1, \mu_2]$ (as per eqns. (3.21) and (5.7)) is dictated by the coupled system of equations:

$$\dot{\boldsymbol{\mu}} - \boldsymbol{\ell} \boldsymbol{\mu} - \boldsymbol{\mu} \boldsymbol{\ell}^T + k_T \left(\boldsymbol{\mu} - 2 \frac{\boldsymbol{I}}{\text{Tr}(\boldsymbol{\mu}^{-1})} \right) = 0 \quad \text{and} \quad \sigma_2 = 0$$
 (5.9)

These equations, combined with a time integrator, may then be solved numerically for the unknowns: μ_1 , μ_2 , and ℓ_2 . Refer to Appendix D.3 for more details. With this, it is then possible to reconstruct the stress tensor using eqn. (4.6).

Using the above procedure, we consider a loading history where the original domain is deformed, starting at time t=0 up to a stretch ratio $\lambda_1=2$, at which point it becomes longitudinally constrained ($\ell_1=0$) to allow for relaxation. Fig. Ω_1 shows the longitudinal stress σ_1 vs time for different values of the normalized strain rate (or Weissenberg number) $W=\ell_1/k_T^0$. For fast loading case W=10, tissue relaxes quickly initially due to an increased rearrangement rate ($k_T>>k_T^0$). The model further predicts that as the strain rate decreases, the tissue is able to relax stress during the loading phase, which results in a reduction of the effective tissue stiffness. In the relaxation stage, the model further predicts a non-exponential stress decay with time. This non-linear viscoelastic response is a signature of the dependence of the overall relaxation rate (d_T) on the cell shape anisotropy χ (whose evolution is depicted in Fig. Ω).

(b.) Nonlinear rheology. The rheology of viscoelastic media (i.e. its flow under shear stress) is usually characterized by the relationship between shear stress and shear strain rate measured in rheometry creep experiments. In confluent tissues, this ability to creep is enabled by cell intercalation. In this context, Duclut et al. (2021) used vertex-based simulations to explore the rheological response of confluent cells with heterogeneous and fluctuating line tensions $\Lambda_{IJ}(t)$. In this example, we reproduce the loading conditions considered in the above study as follows. We again consider a homogeneous domain whose motion is recorded in a 2D Cartesian coordinate system with unit basis vectors $\{e_1, e_2\}$. This domain is subjected to the deformation- and velocity-gradients:

$$\boldsymbol{F} = \begin{bmatrix} 1 & \gamma \\ 0 & 1 \end{bmatrix} \quad \text{and} \quad \boldsymbol{\ell} = \dot{\boldsymbol{F}} \boldsymbol{F}^{-1} = \begin{bmatrix} 0 & \dot{\gamma} \\ 0 & 0 \end{bmatrix}, \tag{5.10}$$

respectively where γ is the shear deformation. In this case, the velocity gradient is entirely determined and the time evolution of the elastic tensor μ is given by the first equation in eqn. (5.9). As before, this equation can be numerically integrated to determine the elastic tensor and stress over time. Fig. 6c. depicts the steady-state cell elongation μ_{12}^{ss} vs strain rate $\dot{\gamma}$ for different rearrangement rates k_T^0 . The inset of Fig. 6d. shows that the steady state is usually preceded by a transient evolution of the elastic tensor during which the shear rate $(\dot{\gamma})$ and the internal rearrangements rate d_T are not equal. As the system reaches a dynamical equilibrium, the steady state μ_{12}^{ss} shows a decrease in the slope of the curves, which is a hallmark of tissue fluidization (Krajnc et al.) (2018). One may also interpret this result as shear thinning whereby the shear viscosity $v = \tau^{ss}/\dot{\gamma}$ decreases with an increase in shear rate. The steady-state shear stress τ^{ss} can be determined from μ_{12}^{ss} using eqn. (4.6). This change in viscosity with strain rate is illustrated in Fig.

6d. These predictions are qualitatively in line with the vertex model results from (Duclut et al., 2021). We also note that the effect of bond-tension fluctuations (represented here by a rise in the rearrangement rate k_T^0) is significant as it results in a more fluidized cell network, again in general agreement with (Duclut et al., 2021).

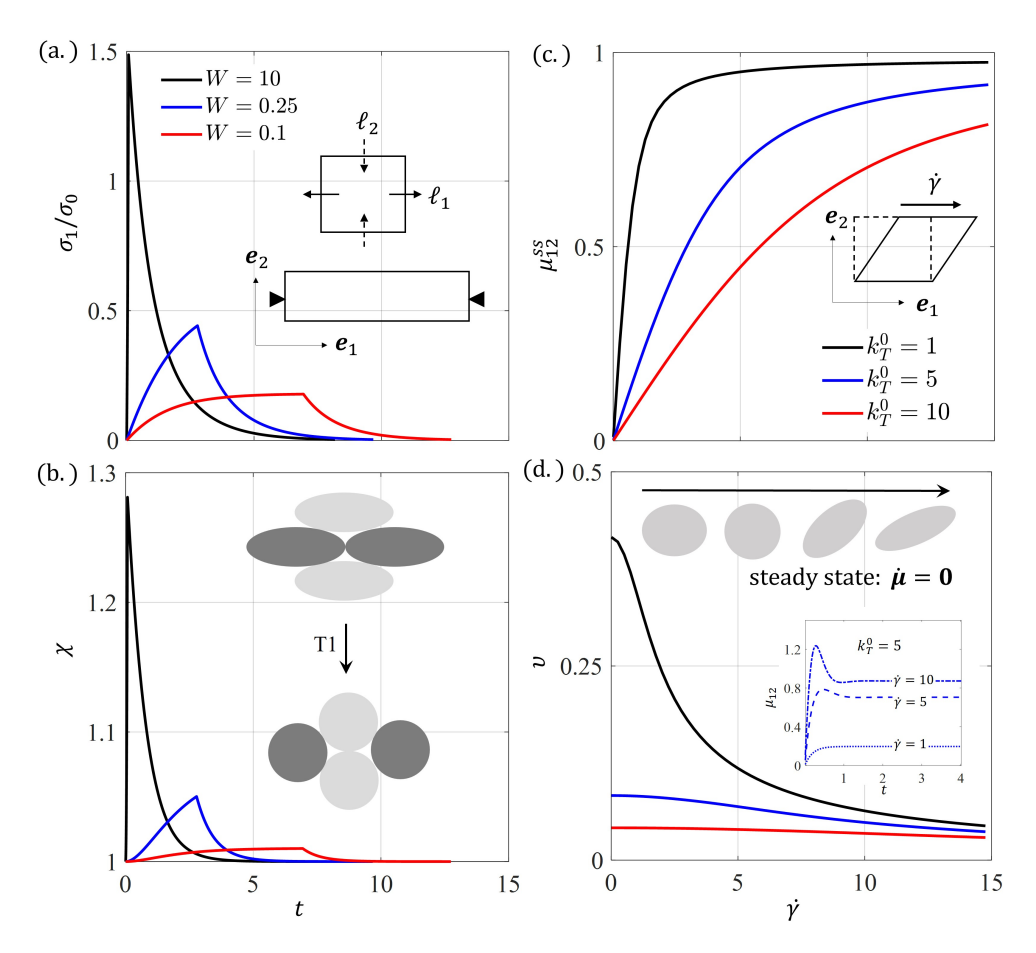


Figure 6: (a.) Passive stress relaxation due to cell rearrangements for different loading rates (W): Tensile stress σ_1/σ_0 vs time t. (b.) Anisotropic strains χ plotted against time t, induce T1 transitions which drive the relaxation response. Time t is measured in units of $k_T^0 = 1$ for the relaxation problem. (c.) 12 component of steady state cell elongation tensor μ^{ss} vs. shear rate $\dot{\gamma}$ and (d.) shear viscosity ν vs shear rate $\dot{\gamma}$ (Inset: μ_{12} vs time t for $k_T^0 = 5$). k_T^0 , $\dot{\gamma}$ and ν are measured in units of frequency $\mathscr{A} = 1$ which sets the time scale for rheology problem. (Simulation parameters: $\bar{\Gamma} = 0.14$, $\bar{\Lambda} = -0.4$. T1 parameters: $\chi_c = 1.1$ and controlling parameter $\frac{\varrho_T}{2\varepsilon} = 1$)

5.2. Cell division

Similar to T1 transitions, the process of cell division induces topological rearrangement that drives tissue rheology as they grow. Unlike T1 transitions, however, cell division is associated with an increase in the nominal cell density C and hence cell number ratio η . As the area A of the parent cell is increased (via growth or external deformation), it divides into two daughter cells, each with area A/2. Fig. 7a. illustrates how new connections amongst daughter cells are created as older ones are destroyed resulting in an overall increase in the nominal segment density c = (z/2)C.

Division criterion. The process of cell division can usually be described by a simple first-order kinetic model with a division rate k_D , such that

$$\dot{\eta}_D = k_D \eta_D \tag{5.11}$$

Experimental observations (Tzur et al., 2009) suggest that the rate of cell division is not constant, but a function of cell size. To capture this mechanism, vertex models employ a probability-based criterion (Xu et al., 2016) to

determine when a specific cell enters mitosis. With this formalism, a cell is allowed to divide only if its current area $A(t) = \zeta(t)A(0)$ is greater than some threshold area $A^* = \zeta^*A(0)$. This criterion, therefore, sets the yield behavior for division as observed in Xu et al. (2015). On the continuum level, this criterion can be expressed in terms of the dimensionless cell area $\zeta = A/A(0)$ as a probability function P_D for cell division:

$$P_D(\zeta) = 1 - \exp\left[-\varrho_D \zeta_0 \left(\zeta - \zeta^*\right)\right] \quad \text{if} \quad \zeta > \zeta^* \tag{5.12}$$

and $P_D(\zeta) = 0$ otherwise. The unit-less parameter ϱ_D controls the rate at which cell division is affected as the cell area approaches its threshold value. Following this probabilistic model (see Fig. 7b.), it is now possible to define a variable representing division rate as:

$$k_D(\zeta) = k_D^0 P_D(\zeta) \tag{5.13}$$

where the rate k_D^0 sets the limit on multiplication rate when the cell area far exceeds the division criterion (i.e. $P_D \to 1$).

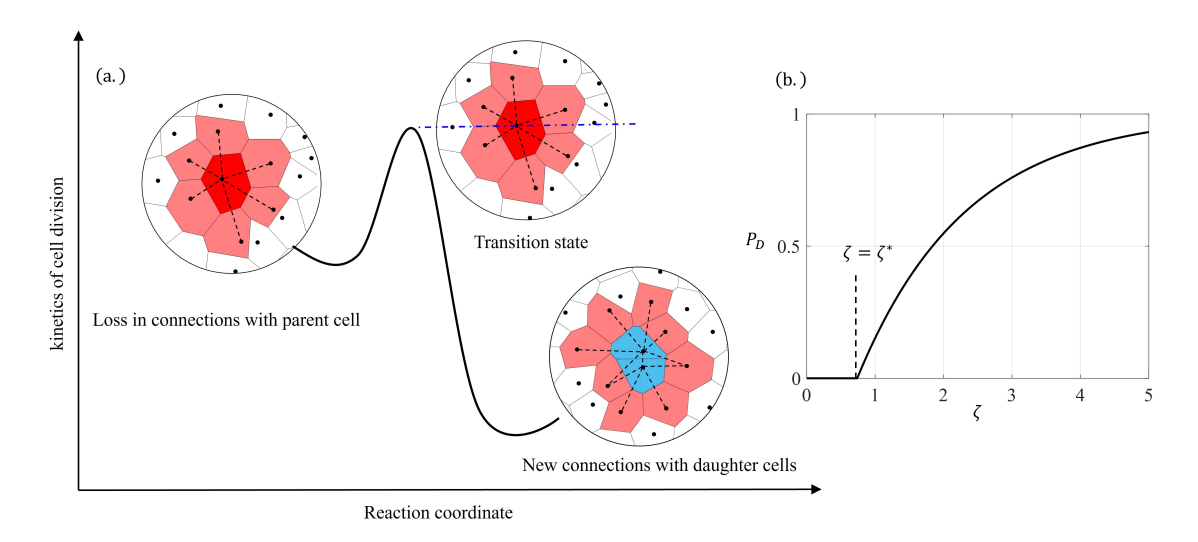


Figure 7: TNT illustration of Cell division: (a.) Cell division results in a net gain of segment vectors. Kinetics of cell division where a cell with $\zeta > \zeta^*$ divides with probability P_D as plotted in (b.)

Rate of inelastic deformation from cell division. The governing equations for cell division involve both a rate-dependent plastic flow d_D and an evolution equation for the cell number ratio (represented by the rate $\dot{\eta}_D$). For this, we start by defining evolution laws for the rates of creation and loss of segment vectors. Supposing the division criteria is satisfied, the rates ξ_l (for segment loss) and ξ_c (for segment creation) are given by:

$$\xi_l(\mathbf{r}) = k_D \left[\frac{z}{2} C \right] p(\mathbf{r})$$
 and $\xi_c(\mathbf{r}) = k_D \left[zC \right] p^*(\mathbf{r})$ (5.14)

In the above expressions, the parameter k_D (eqn. (5.13)) represents the rate of division while the product (z/2)C counts the number of segments lost during the division of C cells per area. Since during division, a single cell (parent cell) is replaced by two new cells (daughter cells), the number of created segments is given by zC (as it appears in the term ξ_c). Finally, the probability densities p and p^* describe the conformation of the segments before and after division, respectively. With these expressions, we find that the overall rates of segment loss and creation are $\Xi_l = k_D(z/2)C$ and $\Xi_c = k_D zC$, respectively. Thus, as expected, the conservation equation (3.14) degenerates to equation (5.11). The associated plastic flow may also be derived from equation (3.20) to find (see Appendix E.1) for details):

$$d_D = k_D (\mu - 2\mu_D) \qquad \text{where} \qquad \mu_D = \frac{1}{m_0} \frac{1}{\zeta_i} \int_{\Omega} p^* \, \boldsymbol{r} \otimes \boldsymbol{r} \, d\Omega \tag{5.15}$$

Equation (5.15) thus entirely determines the plastic flow that originates from cell division, on the condition that the $pdf p^*$ is well defined. We note that to derive this result, we used the fact that cell division must occur without inelastic changes in volume (i.e. $J_i = 0$). Since $J_i = \eta \zeta_i$, this means that:

$$\dot{\zeta}_i = -k_D \zeta_i \tag{5.16}$$

In other words, as cells divide, their average preferred area $\zeta_i A_R(0)$ decreases at rate k_D . This finding is interpreted as a reduction of the average cell size during division. We also show in Appendix E.1 that the condition $\dot{J}_i = 0$ during division requires that:

$$\operatorname{Tr}(\mu_D \mu^{-1}) = 1 \tag{5.17}$$

This condition will be critical to obtain an approximation for the tensor μ_D .

Random and Directed Cell Division. While the pdf p(r) implies that before division, cells are found in the current conformation (described by the current pdf p), the form of the pdf p^* after division relates to the orientation at which cells preferably divide. In this context, Xu et al. (2016) used a vertex model to investigate the effect of the division axis on the stress response of stretched tissue mono-layer. They found that cells dividing along their major axis resulted in cell configurations that were more random and isotropic. By contrast, the average aspect ratio of cells dividing randomly without bias was found to be greater. Motivated by these observations, we now consider two possible situations:

• Unbiased division occurs when cells divide randomly without any preference for the division axis. In this case, we do not observe any change in the average cell shape during division at the level of the population. This implies that we can write $\mu_D = (a_1/J_e)\mu$, where a_1 is a coefficient to be determined. Using the condition in eqn. (5.17), we find $a_1 = J_e/2$ and the plastic flow becomes:

$$d_D = 0 ag{5.18}$$

We, therefore, predict that besides increasing the cell number (and decreasing ζ_i), random cell division has no effect whatsoever on the elastic behavior (i.e. μ) of the cell population. In this case, when cells divide in a random fashion, the change in distribution M due to topological changes is canceled out by changes in the reference cell area. Interestingly enough, cells can still relax stresses owing to decreasing ζ_i as we will see later.

• Directed division occurs when cells preferentially divide along their principal axis. In this case, the elastic tensor after deformation tends to converge back to an isotropic state and we can write $\mu_D = a_2 I$, where the coefficient a_2 is determined to be $a_2 = 1/\text{Tr}(\mu^{-1})$ using condition (5.17). The plastic flow in the event of oriented or biased cell division becomes:

$$d_D = k_D(\zeta) \left(\mu - 2 \frac{I}{\text{Tr}(\mu^{-1})} \right)$$
 (5.19)

In this case, we see that the process of division has the same overall effect as T1 transition on the elastic response of tissue i.e. it does not change the elastic energy of isotropic cells (when $\mu = J_e I$). However, once the cells are deformed anisotropically then they can relax both pressure and deviatoric stresses.

Dissipation due to cell division: Just like T1 transitions, cell divisions can be active or passive depending on the driving forces, whether external or internal. In this section, we will look at passive cell divisions, for which the corresponding dissipation \mathcal{D}_D will be derived, and later in section 5.3 we will explore the active nature of divisions stemming from growth induced forces. Passive cell divisions, just like T1 transitions, are also known to relax stresses in tissues. Assuming a fraction ξ of cells divide in a directed manner and the rest $(1 - \xi)$ in random fashion, the dissipation \mathcal{D}_D for such a general case can be derived (see Appendix E.2) as:

$$\mathcal{D}_D = \frac{1}{J_e} \frac{\partial \psi_i}{\partial I_1} k_D \xi \operatorname{Tr} \left(\mu - \frac{2}{\operatorname{Tr}(\mu^{-1})} I \right) + \frac{k_D}{J_e} \psi_i$$
(5.20)

Where the first term, akin to T1 transition, accounts for stress relaxation by restoring the isotropic shape of cells. The second contribution, on the other hand, is what differentiates both the topological transitions - T1 and division, from one another. Passive cell divisions have an additional source of energy dissipation that comes from the change in the inelastic expansion ratio ζ_i . This additional contribution is always greater than or equal to zero and increases with increases in the rate of cell division rate, implying the validity of constitutive relations for cell divisions. Note that when $\xi = 0$ i.e. cells divide along randomly chosen axes, the tissue is still able to relax via cell division owing to this second term. To illustrate this, let us now explore how both of these dissipation sources, one governed by μ and the other by ζ_i , unfold.

5.2.1. Illustrations

In this section, we will study division-driven stress relaxation in two simple cases: (i) Uni-axial tension and (ii) Purely volumetric deformation (dilation). Again, results are qualitatively compared to those obtained from experimental studies and vertex simulations.

Division-driven stress relaxation. Experiments by Wyatt et al. (2015) suggested that the process of cell division can be the source of stress relaxation in stretched epithelial tissues. This was later confirmed by Xu et al. (2016) using vertex simulations. To illustrate the cell division component of our model, we first explore the division-driven stress relaxation problem using the same uni-axial stretch test as in example 5.1.1(a). Depending on whether divisions are random ($\xi = 0$) or oriented ($\xi = 1$), the governing equation (5.9) is rewritten using eqn. (5.19) that has the final form:

$$\dot{\boldsymbol{\mu}} = \boldsymbol{\ell} \boldsymbol{\mu} + \boldsymbol{\mu} \boldsymbol{\ell}^T - \xi k_D \left(\boldsymbol{\mu} - 2 \frac{\boldsymbol{I}}{\text{Tr}(\boldsymbol{\mu}^{-1})} \right) \quad \text{and} \quad \dot{\sigma}_2 = 0$$
 (5.21)

and solved for the unknowns (μ_1, μ_2, ℓ_2) using the same numerical procedure as illustrated for example 5.1.1a. For clarity, we here consider only a high loading rate (i.e. the tissue remains elastic in this phase) and concentrate our discussion on the stress-relaxation results. Figs. and be depict numerical results for the evolution of stress, cell density, and inelastic expansion ratio ζ_i as a function of time in the second stage of the loading history ($\ell_1 = 0$). Results are obtained for three values of the threshold ζ^* appearing in the division criterion (5.12). The model predicts that in contrast to the T1 transitions, cell division results in partial stress relaxation, i.e. the stress plateaus to a finite value at infinite time. This plateau corresponds to the stress at which the volumetric deformation of cells, i.e. ζ , equals the threshold value ζ^* .

Moreover, we also investigate the impact of random cell division (see inset of Fig. 8a.). In this case, we find that stresses relax at a slower rate and cells dissipate less energy. Xu et al. (2016) also observed a similar response, which can be explained by the driving factors of stress relaxation as per our model. In random cell division, the change in ζ_i becomes the only reason for stress reduction since $\mu = FF^T$, whereas directed divisions augment dissipation via a reduction in elastic strain μ .

From a micro-mechanical perspective, the model suggests that stress relaxation is inextricably linked to cell division and the cells' inelastic volumetric expansion ζ_i (through eqns. (5.11) and (5.16) respectively). These measures are illustrated in Fig. 8b., confirming tissue stretch induces two mechanisms. First, a quick rise in cell area at constant density during the fast loading stage, and second, an increase in cell number accompanied by a decrease in their area.

Cell division vs T1 transition. To exemplify the difference between different modes of passive cell rearrangements: T1 transition and cell division, we solve for another boundary value problem in which the tissue is loaded quickly under isotropic deformation gradient $F = diag[\lambda, \lambda]$ and then constrained along both the principal axes. In this case, since the cell deformation is purely volumetric $(\bar{\mu} = I)$, the inelastic flow rates $d_D = d_T = 0$ at all times. Despite this, the tissue is able to relax stresses via cell divisions. The source of this relaxation (see Fig. 8c.,d.) is the resetting of the preferred cell area according to $A_R(t) = \zeta_i A_R(0)$, by cell division. Note that T1 transitions are unable to relax such a hydrostatic stress state ($\sigma = diag[\sigma, \sigma]$). This illustrates how cell divisions differ from T1 transitions, even though both are represented by similar flow rules: d_D and d_T . We also refer to dissipation \mathcal{D}_D (5.20) which in this case becomes $\mathcal{D}_D = \psi_i k_D/J_e$ while for T1 transitions we have $\mathcal{D}_T = 0$. Thus the inclusion of state-variable ζ_i in our stress

tensor (4.6) enables us to predict the differences in the inelastic behavior attributed to these rearrangements, both of which on a macroscopic level satisfy $\dot{J}_i = 0$. In T1 transitions where the condition is satisfied by $\dot{\eta} = \dot{\zeta}_i = 0$, the same condition for cell division is validated through $\dot{\eta}/\eta = k_D$ and $\dot{\zeta}_i/\zeta_i = -k_D$.

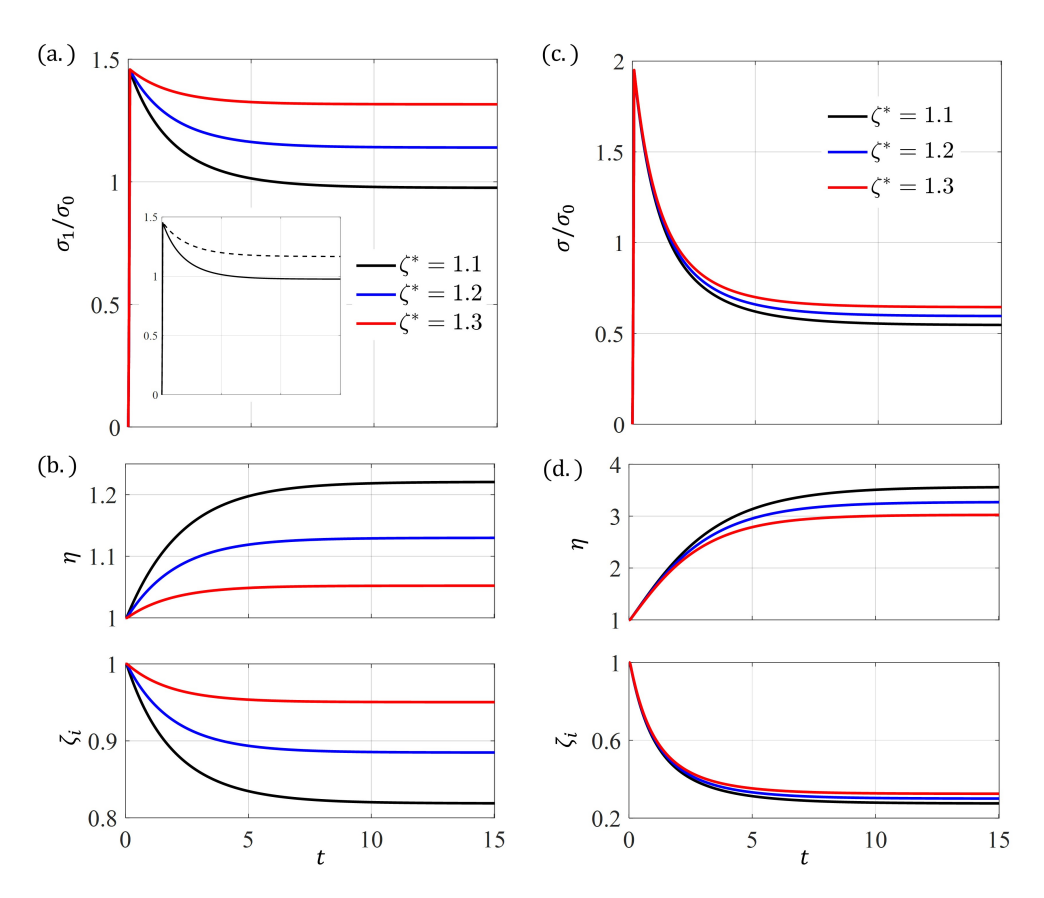


Figure 8: Passive stress relaxation followed by uni-axial stretching: (a.) σ_1/σ_0 vs time t (Inset: σ_1/σ_0 vs t for oriented vs random division) (b.) Cell number ratio η and inelastic expansion ratio ζ_i vs time t. Passive stress relaxation followed by dilational loading: (c.) σ/σ_0 vs t (d.) Cell number ratio η and inelastic expansion ratio ζ_i vs time t. (Simulation parameters: $\bar{\Gamma} = 0.14$, $\bar{\Lambda} = -0.4$, $\varrho_D = 0.63$ and $k_D^0 = 1$, which also sets the time scale for this problem.)

5.3. General cell proliferation

The growth of a confluent cell population typically involves a combination of cell expansion (or an increase in cell volume) and cell division. For this reason, we here split the proliferation plastic flow d_P into a contribution from cell expansion (subscript G) and a contribution from cell division (subscript D):

$$d_P = d_G + d_D \quad \text{and} \quad \dot{\eta} = \dot{\eta}_D \tag{5.22}$$

We have already looked at cell division (d_D and $\dot{\eta}_D$) in the previous section. Let us now understand cell growth or cell expansion which corresponds to a steady increase in a cell's volume over time.

Cell expansion law. Within the vertex model framework, cell expansion is achieved by increasing the preferred area A_R of randomly chosen cells according to a linear kinetic law. Without loss of generality, we here follow the exponential growth law inspired by the work of Barton et al. (2017) in the form $\dot{A}_R = k_G A_R$ where k_G is the growth rate. Note that this law describes a change in the cell's reference area (rather than the current area A), which eventually translates into a change in the elastic state and pressure experienced by growing cells. At the continuum scale, the

above relation can thus also be expressed in terms of the inelastic expansion ratio ζ_i (introduced in eqn. (3.8)) as

$$\dot{\zeta}_i = k_G \zeta_i \tag{5.23}$$

With this relation, we are now in a position to write the inelastic plastic strain rate resulting from cell expansion. For this, we first note that cell expansion is not associated with any change in network topology (i.e. the last two terms in eqn. (3.20) must vanish). It is then straightforward to substitute the growth law (5.23) into eqn. (3.20) to extract the inelastic strain rate owing to cell expansion as:

$$d_G = k_G \mu \tag{5.24}$$

Furthermore, cell expansion does not involve any changes in cell number and hence $\dot{\eta}_G = 0$.

Effect of stress on cell expansion. The assumption of a constant expansion rate is usually inaccurate when cells are mechanically constrained. In fact, the expansion of mechanically constrained cell aggregate systems (tumor spheroids for instance) has been found to be inhibited by stress (Helmlinger et al.) [1997]. This mechanotransduction effect can be accounted for in the vertex model by adjusting the rate k_G to the hydrostatic pressure $\bar{\sigma} = \text{Tr}(\sigma)$ felt by cells, yielding (Ambrosi and Mollica) [2004]:

$$k_G(\bar{\sigma}) = k_G^0 \exp\left[-\left(\frac{\bar{\sigma}}{\bar{\sigma}_0}\right)^2\right]$$
 (5.25)

where k_G^0 is the pressure-free rate of growth and $\bar{\sigma}_0$ is a constant that acts as a threshold pressure beyond which the growth rate decreases rapidly.

Note on ζ_0 : Recall that while deriving the above equations, we assumed that the residual elastic deformation ζ_0 remains constant. Although cell proliferation may affect it, we simplified our analysis by disregarding any influence of d_P on ζ_0 . What this implies is that cell proliferation does not change normalized cell properties $\bar{\Gamma}$ and $\bar{\Lambda}$. As a result of which the preferred shape index $p_p = -\bar{\Lambda}/2\bar{\Gamma}$ remains unchanged as well. In fact, our assumption on constant $\bar{\Gamma}$ and $\bar{\Lambda}$ imply that absolute values of contractility Γ and junction tension Λ evolve with ζ_i according to:

$$\Gamma(t) = \bar{\Gamma}K\zeta_i(t)A_R(0) \quad \text{and} \quad \Lambda(t) = \bar{\Lambda}K(\zeta_i(t)A_R(0))^{3/2}$$
 (5.26)

General response: For the sake of completeness, we will now consider a case where cells grow, divide, and intercalate simultaneously. Moreover, the multi-cellular system may be under the application of external forces due to mechanical confinement. Let us now see how different continuum-level quantities and ISVs evolve under this situation:

We start by inelastic cell expansion ratio ζ_i , whose general evolution law can be written by combining eqns. (5.23) and (5.16) as:

$$\dot{\zeta}_i = \left[k_G(\bar{\sigma}) - k_D(\zeta) \right] \zeta_i \tag{5.27}$$

Using the above, the volumetric inelastic deformation $J_i = \eta \zeta_i$ can be found to evolve as:

$$\dot{J}_i = k_G J_i \tag{5.28}$$

where again we have used the fact that only cell division results in a change in η according to $\dot{\eta}/\eta = k_D$. Relation (5.28) underlines that it is the cell expansion term k_G that drives inelastic volumetric deformation at the macroscopic level. Additionally, k_G , which characterizes an active phenomenon at the cell level, can be linked to the system's macroscopic rate of mass increase as well as growth deformation tensor F_g . For the sake of consistency with existing literature, particularly in continuum growth mechanics, we decompose the total velocity gradient into two components: growth ℓ_g and non-growth $\bar{\ell}$. The growth velocity gradient ℓ_g captures the rate at which tissue expands due to *volumetric*

growth. Tissue can also grow through *densification*, which involves an increase in mass density ρ_i . The non-growth component $\bar{\ell}$ would then encapsulate elastic deformation as well as topological rearrangements, both of which do not contribute to altering the system's mass. Following this decomposition of ℓ and flow rates d_T , d_D , d_G , the complete form of $\mathcal{L}(\mu)$ can now be explicitly written as:

$$\dot{\mu} = \bar{\ell}\mu + \mu\bar{\ell}^T - d_T - d_D - d_G + \ell_g\mu + \mu\ell_g^T \tag{5.29}$$

In such a general scenario, we observe that while inelastic processes occur concurrently and interact with one another, they remain independent, and hence all the equations derived in this study continue to hold true. One example of the mechanotransduction effect where one inelastic process affects another is the possibility of topological rearrangements relaxing stresses (σ) which in turn facilitates growth k_G as per eqn. (5.25). Using this and eqn. (3.28), the general form of Clausius-Duhem inequality can be written as:

$$\mathscr{D} = \left(\sigma - \frac{2}{J_e} \frac{\partial \psi_i}{\partial \mu} \mu\right) : \bar{\ell} + \frac{1}{J_e} \frac{\partial \psi_i}{\partial \mu} : d_T + \frac{1}{J_e} \frac{\partial \psi_i}{\partial \mu} : d_D + \frac{1}{J_e} \frac{\partial \psi_i}{\partial \mu} : \left(d_G - 2\ell_g\right) + \frac{\psi_i}{J_e} \frac{\dot{\rho}_i}{\rho_i} - \frac{\psi_i}{J_e} \frac{\dot{\zeta}_i}{\zeta_i} + \sigma : \ell_g \ge 0 \quad (5.30)$$

Here, the first term represents tissue elasticity and does not contribute towards dissipation. The second and third terms account for viscous dissipation arising from T1 transitions and cell division, respectively. The fourth term allows for a constitutive relation that connects macroscopic volumetric growth ℓ_g with cell-level growth d_G . The fifth term characterizes growth resulting from densification. The sixth term depends on the rate of inelastic expansion ζ_i and includes cell growth as well as division. On the one hand, where no active processes are present ($k_G = 0, \dot{\rho}_i = 0$), this term contributes to dissipation as we can see from eqn. (5.20). On the other hand, where there is no elastic deformation (i.e. during free homogeneous growth), this term combines with the densification term to provide another constitutive relation between both ρ_i and ζ_i . We will explore this in more detail in the next section. The final term can be expressed as a Mandel stress (Huang et al., 2021), depicting the work done by internal forces due to growth.

5.3.1. Illustration

We now use the proliferation model to explore the mechanics of confluent cell population in a simple case of free proliferation or stress-free growth.

Free proliferation dynamics. In this example, we evaluate the model's prediction for mechanically unconstrained tissue proliferation. We analyze the time-dependent behavior of geometrical tissue expansion, cell density, and size as per the model's equations (5.19), (5.24) and (5.27). We observe that, in stress-free conditions, the hydrostatic pressure $\bar{\sigma} = 0$ and, as a result, the cell expansion rate remains constant ($k_G = k_G^0$) as per eqn. (5.25). However, the rate of cell division is altered due to changes in cell size ζ . Even though cells are dividing, the inelastic flow $d_D = 0$ due to the isotropy of cells. Similarly $d_T = 0$ as well. To determine the growth-induced velocity gradient $\ell = \ell_g$ we now substitute $d_P = 0$, $d_T = 0$ and $d_G = k_G^0 I$ in equation (3.21) to evaluate the overall tissue expansion. Moreover, since there is no elastic deformation during stress-free growth, the elastic tensor μ remains equal to the identity I, and we can use the condition $\dot{\mu} = 0$ to derive:

$$\ell_g = \frac{k_G^0}{2} I \implies F_g = \exp\left(\frac{k_G^0}{2} t\right) I$$
 (5.31)

Here, the resulting isotropic growth-induced deformation gradient F_g was obtained by straightforward integration of ℓ_g . We, therefore, predict an exponential increase in tissue size, whose growth rate is entirely determined by the expansion rate of individual cells, but not their division rate.

To follow the evolution of the average cell area during growth, we now invoke eqn. [5.27] whose solution is determined through a classical time integration scheme. Figure [9]a. presents the evolution of cell area ζ in time, where it is clear that the solution converges to a steady state (that is a solution of $\dot{\zeta} = 0$) provided $k_G^0 < k_D^0$. Using eqns. (5.13) and (5.12), the steady state value of dimensionless cell size $\zeta = A/A(0)$ has the closed form:

$$\zeta^{eq} = \zeta^* - \frac{1}{\varrho_D \zeta_0} \ln \left(1 - \frac{k_G^0}{k_D^0} \right)$$
 (5.32)

Further since $\zeta_e = 1$, we have $\zeta = \zeta_i$ and hence $\zeta_i^{eq} = \zeta^{eq}$. The relation (5.32) shows how various model parameters affect cell area. For instance, the division threshold ζ^* tends to delay the division process, resulting in a higher steady-state cell area. However, once the division process starts then homeostasis is achieved more rapidly. Finally, knowing the area of the grown tissue (from $J = J_i = J_g = |F_g|$), the evolution law for cell number ratio (3.8) quickly gives the solution:

$$\eta = \frac{1}{\zeta_i} \exp(k_G^0 t) \tag{5.33}$$

Note that this exponential growth is consistent with the evolution of F_g at steady state. Indeed, for a constant size of cells, the only means to produce *volumetric* growth is to increase cell number. Thus *volumetric* growth and cell count must follow similar dynamics. Generally, these results can be compared to the quasi-static vertex model study by Farhadifar et al. (2007) that considered tissue proliferation where the zero stress condition was maintained by minimizing energy at every time step. While the dominant mode of stress relaxation in their vertex model study was local cell rearrangements (T1 and T2), on a continuum level this relaxation can be attributed to changes in cellular properties Γ and Λ , as given by eqn. (5.26), that ensure that tissue remains stress-free. In line with the outcomes of vertex model results, we found that unconstrained proliferating tissues achieve homeostasis concerning cell area, leading to a steady state energy per cell (\mathcal{E}/η), as k_D eventually converges to k_G^0 (see Fig. [9b.). However, if $k_G^0 > k_D^0$, no homeostasis can be attained since, in this scenario, cell growth is unlimited due to $\dot{\zeta}_i > 0$ consistently. We now use the general form of Clausius-Duhem inequality (5.30) to gain further insights. Since in this illustration we model stress-free growth where $\sigma = 0$, $\mu = I$, and $\ell_g = d_G/2 = k_G^0/2$, the dissipation \mathcal{D} in eqn. (5.30) should vanish which results in:

$$\frac{\dot{\rho}_i}{\rho_i} = \frac{\dot{\zeta}_i}{\zeta_i} \tag{5.34}$$

The model predicts an intriguing scenario where the overall growth (i.e. increase in mass) during the transient phase encompasses not only a *volumetric* aspect but also incorporates a *densification* component. Only after homeostasis is achieved the growth becomes completely *volumetric*. Conventional continuum growth theories founded on $F = F_e F_g$ ignore *densification* and assume just *volumetric* growth. Our cell-proliferation-based model effectively captures both *volumetric* and *densification* contributions to free growth, as demonstrated by this illustration.

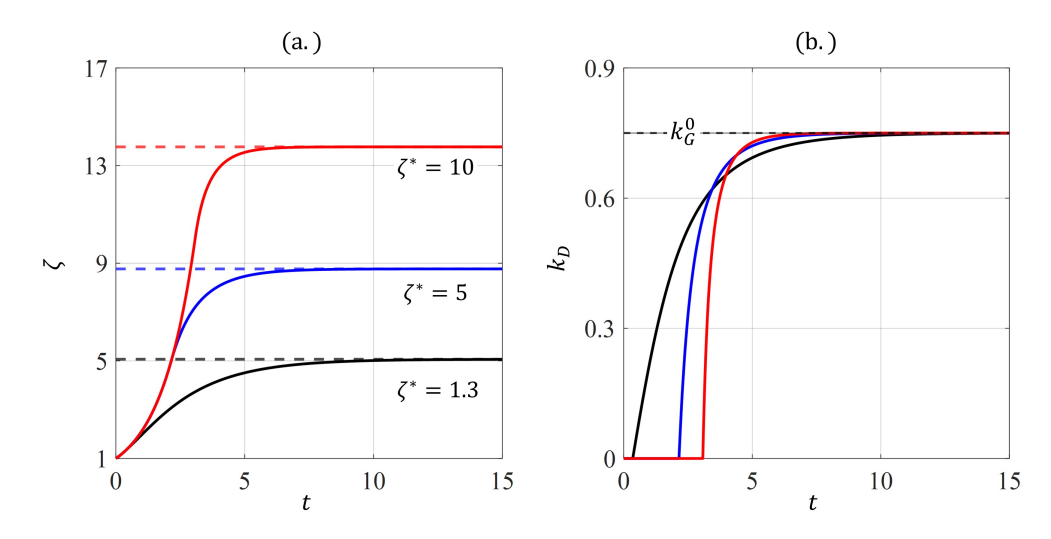


Figure 9: (a.) The transient as well as steady-state response of dimensionless cell area ζ where the numerical solutions in steady-state coincide with their corresponding analytical values of ζ^{eq} (corresponding dashed lines). (b.) Cell multiplication rate k_D vs time t. (Simulation parameters: $\bar{\Gamma} = 0.14$, $\bar{\Lambda} = -0.4$, $\varrho_D = 0.63$, $k_D^0 = 0.75$ and $k_D^0 = 1$, which also sets the time scale for this problem.)

6. Summary and Conclusion

To summarize, we developed a statistically-based continuum model for the rheology and growth of confluent cell monolayers based on cell-based rules from the vertex model. The model is thus able to describe the macroscopic evolution laws for a tissue whose dynamics is driven by cell deformation, intercalation, expansion, and division. Eventually, the formulation is expressed in terms of the elastic tensor μ that represents the average elastic deformation of cells in the tissue. We showed that the time evolution of this tensor is dictated by the competition between several kinetic processes: the rate of tissue deformation, the rate of cell expansion, the rate of cell division, and the rate of T1 transition. Notably, the last three rates are not only governed by biological processes but they are also an implicit function of the physical state of cells and their level of hydrostatic pressure. Thus, cell expansion decreases with the level of hydrostatic pressure, cell division occurs for large cell areas while T1 transition drastically increases when cells experience shear deformation. These dependencies create an interplay between each process, in which each mechanism communicates with the other via the development of tissue stress and deformations. Each effect in isolation was illustrated in simple problems, ranging from the nonlinear rheology of tissues to the relationship between tissue growth and cell proliferation.

The proposed approach can be distinguished from existing continuum growth models by its close proximity with cellular-level mechanisms, enabling deeper exploration of the role of microscopic features on overall growth. We note here that even though the mathematical structure of the model is close to that formulated by Ishihara et al. (2017), the main focus here lies on understanding the consequences of proliferation rules, like those employed in vertex models, on the principles of growth physics. We also highlight that these types of models are only valid when a large number of cells comprise the tissue, such that the concept of an average field remains meaningful. It also assumes that the deformation field remains continuous across the tissue. In other words, the continuum model cannot capture finite-size effects such as the localization of events (growth, division, intercalation) in regions containing a limited number of cells. In this situation, discrete models like vertex simulations would be more appropriate. For clarity, we here only included the most salient features that are considered in vertex simulations and more accurate models may be considered to describe both the elasticity and the inelastic processes in these tissues. For instance, the nonlinear elasticity (strain stiffening) elasticity of cells could also be considered following previous work on polymer mechanics (Vernerey, 2018). Regarding inelastic processes, additional mechanisms can be included such as cell apoptosis (commonly called T2 Transitions in vertex models) and other types of cell rearrangements such as rosette formation (Fletcher et al., 2014). Furthermore, the intrinsic viscoelasticity of the cell cytoskeleton (Janshoff, 2021) and that of junctions (Clément et al., 2017) as well as extracellular matrix were not considered here, but could be included in future studies if they become an important player to the tissue's time dependence. The extension of this model to three-dimensional confluent tissues is also desirable for its application to spheroids (Kulwatno et al., 2021) and other types of 3D organoids (Rozman et al., 2020). This will entail simply redeveloping elastic energy for three-dimensional cells, whose average shape would be represented by an ellipsoid (in contrast to an ellipse in 2D). The constitutive laws for the inelasticity model can also be extended in a straightforward manner.

As a final remark, the development of refined continuum models will be essential to understand both qualitatively and quantitatively the feedback between mechanics and biology during disease and development (Friedl and Gilmour, 2009). Today there is a significant effort to understand these dynamics from an experimental perspective with the development of techniques that are increasingly accurate in measuring features at the cell level (Fernandez-Gonzalez et al., 2009; Harris et al., 2012). In parallel, it is now possible to better control the mechanical environment of these cells, their dynamics, and collective interactions through the external stimulus to explore organoid development in vitro (Rossi et al., 2018). Combined with finite element simulations, the proposed model could be valuable in assisting and guiding these efforts.

Acknowledgements

FJV gratefully acknowledges the support of the National Science Foundation under Award No. 2135057. The content is solely the responsibility of the authors and does not necessarily represent the official views of the National Science Foundation.

Appendix A. Mean cell conformation

Appendix A.1. Coarse-graining

The mean cell area (A) and perimeter (L) can be estimated from confidence ellipse as shown in Fig. A1

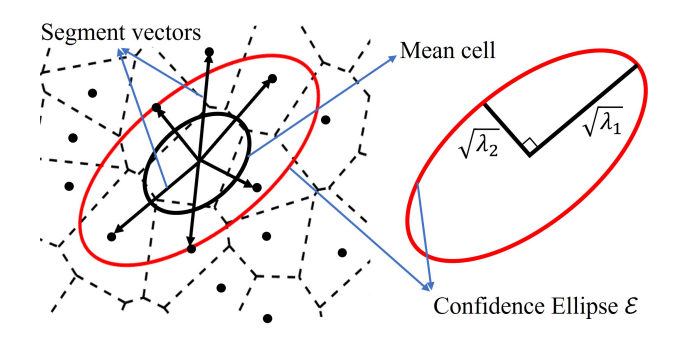


Figure A1: Schematic of approximating mean cell geometry from confidence ellipse

Let a general covariance matrix \mathbf{M} be given by a symmetric tensor: $\mathbf{M} = \begin{bmatrix} a_{11} & a_{12} \\ a_{12} & a_{22} \end{bmatrix}$ or in principal coordinates $\mathbf{M} = \begin{bmatrix} \lambda_1 & 0 \\ 0 & \lambda_2 \end{bmatrix}$ where λ_1 and λ_2 are the eigen values of \mathbf{M} . Area of confidence ellipse \mathcal{E} is $= \pi \sqrt{\lambda_1 \lambda_2} = \pi \sqrt{a_{11} a_{22} - a_{12}^2} = \pi \sqrt{|\mathbf{M}|}$ and the corresponding perimeter is $= 2\pi \sqrt{\frac{\lambda_1 + \lambda_2}{2}} = 2\pi \sqrt{\frac{a_{11} + a_{22}}{2}} = 2\pi \sqrt{\frac{\text{Tr}(\mathbf{M})}{2}}$. The area A and perimeter L of mean cell can then be estimated as:

$$A \propto \pi \sqrt{|M|}$$
 and $L \propto 2\pi \sqrt{\frac{\text{Tr}(M)}{2}}$ (A.1)

As we will develop our constitutive laws in terms of normalized quantities, the proportionality constants in eqn. (A.1) do not impact the model in any way. Thus, for the sake of facilitating equations, they are taken to be equal to 1.

Appendix A.2. Compatibility constrained condition

Consider a general elliptical cell with semi-major axes a and b. The area and perimeter for this ellipse are given by:

$$A = \pi ab$$
 and $L = 2\pi \sqrt{\frac{a^2 + b^2}{2}}$ (A.2)

If $A = A_R$ and $L = L_R$, then Using the above relation (A.2), the target/preferred shape index p_p can be calculated as:

$$p_p = \frac{L_R}{\sqrt{A_R}} = 2\sqrt{\pi} \sqrt{\frac{a/b + b/a}{2}}$$
 (A.3)

Since a and b are always positive, hence, $a/b + b/a \ge 2$ which results in the required condition:

$$p_p \ge 2\sqrt{\pi} \tag{A.4}$$

Appendix B. Evolution of cell network statistics

Appendix B.1. Time evolution of nominal segment distribution density

In order to derive an expression for $\dot{\phi}$, we will draw parallels from the equations frequently used in fluid dynamics. We will see how the treatment of segment vectors within Ω is very similar to that of fluid flow. The main difference will be instead of formulating equations in some physical Cartesian coordinate system (x, y, z) as we do in fluid dynamics, we will focus on our conformation space Ω which has (r_x, r_y) as its basis vectors. Fundamental physical principles such as mass conservation and momentum conservation can be expressed in various forms depending on the approach we employ to study fluid flow. Here we will implement the fixed finite control volume approach that results in an integral and conservative form of the governing equation. We then follow the given steps:

1. Let us first define a finite control volume (CV) given by \mathcal{V} and its corresponding control surface (CS) given by S as shown in Fig. A2. This CV is fixed in the space and fluid is flowing past through it. A similar analogy can be made in the case of TNT where finite domain ω , equivalent to \mathcal{V} , is fixed in the conformation space Ω and bounded by boundary b, equivalent to control surface S.

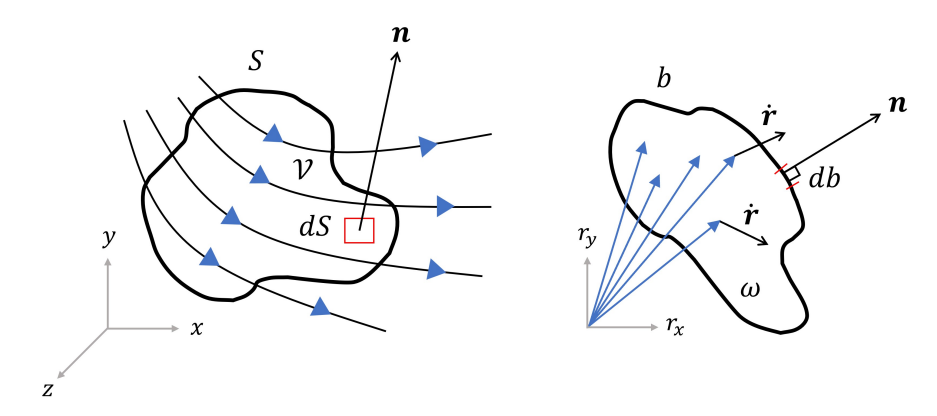


Figure A2: Comparison of fluid dynamics with transient network theory for cells. A fixed control volume approach in fluid dynamics is used to find the governing equation for the conservation laws of fundamental physical principles. Here we will apply the methodology based on the continuity equation (conservation of mass) to derive the Fokker-Planck equation which is basically the conservation equation for the number of segment vectors within ω .

- 2. Let the fluid velocity field be given by $V = [V_x(x, y, z, t), V_y(x, y, t), V_z(x, y, z, t)]$. This is basically the velocity of a fluid particle flowing through the point (x, y, z) at any time t. In conformation space, the flow velocity can be interpreted as the rate of deformation of segment vectors, $\dot{r} = [\dot{r_x}, \dot{r_y}]$. Each point in ω , that corresponds to the head of vector r, can be thought of as a fluid particle that is moving at velocity \dot{r} . Hence vectors can enter and leave the domain ω as a result of deformation.
- 3. Applying conservation of mass for the fluid within \mathcal{V} , we can write:

Net mass of fluid flow through S into $\mathcal{V}(Q)$ = time rate of increase of mass inside $\mathcal{V}(R)$

We can write a similar conservation equation for the number of segment vectors within ω :

Net influx of segment vectors through b into ω (Q) = time rate of increase of segment vectors inside ω (R) (B.1)

4. The mass flow of fluid crossing a fixed surface per unit of time is given by $\rho V \cdot n \, dS$ where $\rho(x, y, z, t)$ is the mass density and n is the outward normal to elementary surface area dS. By convention when fluid enters the CV, the flux is negative and vice-versa in case the fluid leaves the domain. Hence:

$$Q = -\iint_{S} \rho \mathbf{V} \cdot \mathbf{n} \, dS \implies Q = -\iiint_{\mathcal{V}} \nabla \cdot (\rho \mathbf{V}) \, d\mathcal{V}$$
 (B.2)

Since in our TNT, the density of segment vectors in conformation space is given by ϕ , we can write an equivalent form of eqn. B.2 as:

$$Q = -\int_{b} \phi \dot{\mathbf{r}} \cdot \mathbf{n} \, db \implies Q = -\int_{\omega} \nabla \cdot (\phi \dot{\mathbf{r}}) \, d\omega \tag{B.3}$$

5. The total mass of fluid within CV (\mathcal{V}) is given by: $\iiint_{\mathcal{V}} \rho \, d\mathcal{V}$ and the corresponding rate of increase, R, will be $\frac{\partial}{\partial t} \iiint_{\mathcal{V}} \rho \, d\mathcal{V}$. Analogously, the time rate of increase of the number of segment vectors within ω is:

$$R = \frac{\partial}{\partial t} \int_{\Omega} \phi \, d\omega \implies R = \int_{\Omega} \frac{\partial \phi}{\partial t} \, d\omega \tag{B.4}$$

6. The conservation in the number of segment vectors can now be written (R = Q) as:

$$\int_{\omega} \frac{\partial \phi}{\partial t} d\omega = -\int_{\omega} \nabla \cdot (\phi \dot{\mathbf{r}}) d\omega \tag{B.5}$$

which is equivalent to the mass conservation equation of fluid. But unlike CV for the fluid case where extra mass can not be created within \mathcal{V} , nor any mass can get destroyed, new segment vectors can appear in our ω as a result of topological transitions. At the same time, some segment vectors can get lost or annihilated from the domain. Hence eqn. B.5 will be valid only in networks where cell rearrangements are absent. In order to account for these rearrangements we simply add the sink and source terms:

$$\int_{\omega} \frac{\partial \phi}{\partial t} d\omega = -\int_{\omega} \nabla \cdot (\phi \dot{\mathbf{r}}) d\omega + \int_{\omega} \xi_c d\omega - \int_{\omega} \xi_l d\omega$$
 (B.6)

7. The first term on the right-hand side (*RHS*) of the above equation can be expressed in terms of macroscopic velocity gradient $\ell = \ell_{ij}$ using affine kinematics $\dot{r}_i = \ell_{ij} r_j$:

$$\nabla \cdot (\phi \dot{\boldsymbol{r}}) = \dot{r}_i \frac{\partial \phi}{\partial r_i} + \phi \left(\ell_{ii} + r_i \frac{\partial \ell_{ji}}{\partial r_j} \right)^0 \tag{B.7}$$

Since ℓ is uniform throughout the conformation space, its partial derivatives w.r.t r vanish. The first term on RHS can be written in a tensor form as:

$$\dot{r}_i \frac{\partial \phi}{\partial r_i} = \left(\frac{\partial \phi}{\partial \mathbf{r}} \otimes \mathbf{r}\right) : \boldsymbol{\ell}$$
(B.8)

8. Finally substituting eqns. (B.8) and (B.7) in eqn. (B.6) and localizing it we get the required time-evolution equation for our Nominal segment density (ϕ) as:

$$\frac{\partial \phi}{\partial t} = -\ell : \left(\frac{\partial \phi}{\partial \mathbf{r}} \otimes \mathbf{r}\right) - \text{Tr}(\ell) \phi + \xi_c(\mathbf{r}) - \xi_l(\mathbf{r})$$
(B.9)

Appendix B.2. Time evolution of nominal cell density C

Here we derive an expression for \dot{C} . We have already seen:

$$C = \frac{2}{z} \int_{\Omega} \phi \, d\Omega \implies \dot{C} = \frac{2}{z} \int_{\Omega} \frac{\partial \phi}{\partial t} \, d\Omega \tag{B.10}$$

Substituting eqn. (B.9) in eqn. (B.10) we get:

$$\dot{C} = -\frac{2}{z} \int_{\Omega} \boldsymbol{\ell} : \left(\frac{\partial \phi}{\partial \boldsymbol{r}} \otimes \boldsymbol{r} \right) d\Omega - \frac{2}{z} \int_{\Omega} \operatorname{Tr}(\boldsymbol{\ell}) \phi d\Omega + \frac{2}{z} \int_{\Omega} \xi_{c}(\boldsymbol{r}) d\Omega - \frac{2}{z} \int_{\Omega} \xi_{l}(\boldsymbol{r}) d\Omega$$
(B.11)

$$\dot{C} = -\frac{2}{z} \int_{\Omega} \ell : \left(\frac{\partial \phi}{\partial \mathbf{r}} \otimes \mathbf{r} \right) d\Omega - \text{Tr}(\ell)C + \frac{2}{z} \Xi_c(\mathbf{r}) - \frac{2}{z} \Xi_l(\mathbf{r})$$
(B.12)

Expanding the first term on RHS in index notation:

$$\dot{C} = -\frac{2}{z} \int_{\Omega} \ell_{ij} \frac{\partial \phi}{\partial r_i} r_j d\Omega - \text{Tr}(\boldsymbol{\ell}) C + \frac{2}{z} \Xi_c(\boldsymbol{r}) - \frac{2}{z} \Xi_l(\boldsymbol{r})$$
(B.13)

$$\dot{C} = -\frac{2}{z}\ell_{ij} \int_{\Omega} \frac{\partial (\phi r_j)}{\partial r_i} d\Omega + \frac{2}{z}\ell_{ij} \int_{\Omega} \phi \frac{\partial r_j}{\partial r_i} d\Omega - \text{Tr}(\boldsymbol{\ell})C + \frac{2}{z}\Xi_c(\boldsymbol{r}) - \frac{2}{z}\Xi_l(\boldsymbol{r})$$
(B.14)

The first integrand on *RHS* simply resembles $\nabla \cdot (\phi \mathbf{r})$ which results in :

$$-\frac{2}{z}\ell_{ij}\int_{\Omega}\frac{\partial(\phi r_{j})}{\partial r_{i}}d\Omega = -\frac{2}{z}\boldsymbol{\ell}:\int_{\Omega}\nabla\cdot(\phi r)d\Omega = -\frac{2}{z}\boldsymbol{\ell}:\int_{\partial\Omega}(\phi r)d\Gamma$$
 (using divergence theorem) (B.15)

The reason this integral goes to 0 is that the value of ϕ at boundary $\partial\Omega$, which theoretically lies at infinity, is zero, simply because there would be no segment vectors with ∞ lengths. The second term on *RHS* in eqn. (B.14) simply becomes:

$$\frac{2}{z}\ell_{ij}\int_{\Omega}\delta_{ij}\phi\,d\Omega = \ell_{ij}\delta_{ij}\frac{2}{z}\int_{\Omega}\phi\,d\Omega = \text{Tr}(\boldsymbol{\ell})C \qquad \text{where } \delta_{ij} = \delta_{ji} \text{ is the Kronecker Delta}$$
(B.16)

Substituting eqns. (B.15) and (B.16) in eqn. (B.14) we eventually get:

$$\dot{C} = \frac{2}{z} (\Xi_c - \Xi_l) \tag{B.17}$$

Appendix B.3. Fokker-Planck equation

Substituting $\phi = (z/2)Cp$ in eqn. (B.9), we can write:

$$(z/2)p\frac{\partial C}{\partial t} + (z/2)C\frac{\partial p}{\partial t} = -\boldsymbol{\ell} : \left((z/2)C\frac{\partial p}{\partial \boldsymbol{r}} \otimes \boldsymbol{r} \right) - (z/2)C\operatorname{Tr}(\boldsymbol{\ell})p + \xi_c - \xi_l$$
(B.18)

Dividing above by (z/2)C:

$$p\frac{\dot{C}}{C} + \frac{\partial p}{\partial t} = -\ell : \left(\frac{\partial p}{\partial r} \otimes r\right) - \text{Tr}(\ell)p + \frac{\xi_c}{(z/2)C} - \frac{\xi_l}{(z/2)C}$$
(B.19)

Substitute eqn. (B.17) in (B.19):

$$\frac{\partial p}{\partial t} = -\boldsymbol{\ell} : \left(\frac{\partial p}{\partial \boldsymbol{r}} \otimes \boldsymbol{r}\right) - \text{Tr}(\boldsymbol{\ell})p + \frac{\xi_c - p\Xi_c}{(z/2)C} - \frac{\xi_l - p\Xi_l}{(z/2)C}$$
(B.20)

$$\frac{\partial p}{\partial t} = -\ell : \left(\frac{\partial}{\partial r} \otimes (pr) - p \frac{\partial}{\partial r} \otimes r\right) - \text{Tr}(\ell)p + \frac{\xi_c - p\Xi_c}{(z/2)C} - \frac{\xi_l - p\Xi_l}{(z/2)C}$$
(B.21)

Since $\frac{\partial}{\partial r} \otimes r = I$ and $\ell : I = \text{Tr}(\ell)$ where I being the identity tensor, we get the evolution equation of probability density, a.k.a, the Fokker-Planck equation as:

$$\frac{\partial p}{\partial t} = -\ell : \left(\frac{\partial}{\partial r} \otimes (pr)\right) + 2\frac{\xi_c - p\Xi_c}{zC} - 2\frac{\xi_l - p\Xi_l}{zC}$$
(B.22)

Note that nominal cell density $C = \eta C(0)$.

Appendix B.4. Relative deformation of mean cell

Recalling A(t), $A_i(t)$ and A(0) are the mean cell areas in $\mathcal{B}(t)$, $\mathcal{B}_i(t)$, and \mathcal{B}_0 , respectively, and using $A_i(t) = \zeta_0 A_R(t)$, where $A_R(t)$ is the current preferred cell area, we can write:

$$\frac{A}{A_i} = \zeta_e \implies \frac{A}{A_R} = \zeta_0 \zeta_e \tag{B.23}$$

Now for finding the perimeter, which is given by $L = 2\pi \sqrt{\text{Tr}(M)/2}$, we use eqn. (3.10) in the main text to write:

$$L = 2\pi \sqrt{\frac{\zeta_i m_0 I_1}{2}} \tag{B.24}$$

In the intermediate state \mathcal{B}_i , we have perimeter $L_i = 2\pi \sqrt{\zeta_i m_0}$ which yields:

$$\frac{L}{L_i} = \sqrt{\frac{I_1}{2}} \tag{B.25}$$

Also since in the state \mathcal{B}_i , the mean cell is isotropic, we can write $L_i = 2\sqrt{\pi A_i}$. This L_i can further be related to the current value of preferred perimeter $L_R = p_p \sqrt{A_R}$ as:

$$\frac{L_i}{L_R} = \frac{2}{p_p} \sqrt{\frac{\pi A_i}{A_R}} = \frac{2}{p_p} \sqrt{\pi \zeta_0} \tag{B.26}$$

From eqns. (B.25) and (B.26) we get:

$$\frac{L}{L_R} = \frac{2}{p_p} \sqrt{\frac{\pi \zeta_0 I_1}{2}} \tag{B.27}$$

Appendix C. Derivation for Cauchy stress tensor σ

For a perfectly elastic case where $\dot{\mu} = \ell \mu + \mu \ell^T$ and $\dot{\rho}_i = 0$ and Clausius-Duhem inequality in eqn. (3.27) becomes:

$$\mathscr{D} = \boldsymbol{\sigma} : \boldsymbol{\ell} - \frac{1}{J_e} \dot{\psi}_i = 0 \tag{C.1}$$

Since no inelastic mechanisms are operating, $\dot{\psi}_i = (\partial \psi_i / \partial \mu) : \dot{\mu}$, which when substituted in above equation yields:

$$\sigma: \boldsymbol{\ell} - \frac{1}{J_e} \frac{\partial \psi_i}{\partial \mu} : (\boldsymbol{\ell} \mu + \mu \boldsymbol{\ell}^T) = 0 \implies \left(\sigma - \frac{2}{J_e} \frac{\partial \psi_i}{\partial \mu} \mu \right) : \boldsymbol{\ell} = 0 \implies \sigma = \frac{2}{J_e} \frac{\partial \psi_i}{\partial \mu} \mu$$
 (C.2)

For isotropic elastic solids, ψ_i can be expressed as a function of independent variables or invariants (I_1, I_2, I_3) of our second-order elastic deformation tensor μ . This results in:

$$\frac{\partial \psi_i}{\partial \mu} = \frac{\partial \psi_i}{\partial I_1} \frac{\partial I_1}{\partial \mu} + \frac{\partial \psi_i}{\partial I_2} \frac{\partial I_2}{\partial \mu} + \frac{\partial \psi_i}{\partial I_3} \frac{\partial I_3}{\partial \mu}$$
(C.3)

where the derivatives of invariants are given by:

$$\frac{\partial I_1}{\partial \mu} = I \quad ; \quad \frac{\partial I_2}{\partial \mu} = I_1 I - \mu \quad ; \quad \frac{\partial I_3}{\partial \mu} = I_3 \mu^{-1} \tag{C.4}$$

Using eqns. (C.4) and eqn. (C.3) we get the required expression for our Cauchy stress tensor as:

$$\sigma = \frac{2}{J_e} \left[\frac{\partial \psi_i}{\partial I_1} \mu + \frac{\partial \psi_i}{\partial I_2} (I_1 \mu - \mu \cdot \mu) + \frac{\partial \psi_i}{\partial I_3} I_3 I \right]$$
 (C.5)

Since here we are modeling a two-dimensional tissue layer, therefore in our case $I_2 = I_3$ and $\psi_i(I_1, I_3)$. Consequently, the stress equation becomes:

$$\sigma = \frac{2}{J_e} \left[\frac{\partial \psi_i}{\partial I_1} \boldsymbol{\mu} + \frac{\partial \psi_i}{\partial I_3} I_3 \boldsymbol{I} \right]$$
 (C.6)

Appendix D. Derivations for T1 transition

Appendix D.1. T1 Transition flow rate

An important aspect of T1 transitions in our model is that it does not contribute towards inelastic volume changes i.e. ζ_i remains unaffected in the event of cell intercalations. We use this condition to derive μ_T as follows. In the absence of any other inelastic process, d_D , $d_G = 0$, substituting d_T from eqn. (5.6) in eqn. (3.21) yields:

$$\dot{\boldsymbol{\mu}} = \boldsymbol{\ell} \boldsymbol{\mu} + \boldsymbol{\mu} \boldsymbol{\ell}^T - k_T (\boldsymbol{\mu} - \boldsymbol{\mu}_T) \tag{D.1}$$

Multiplying above equation by μ^{-1} and taking the trace results in:

$$Tr(\dot{\mu}\mu^{-1}) = Tr(\ell) + Tr(\mu\ell^T\mu^{-1}) - 2k_T + k_T Tr(\mu_T\mu^{-1})$$
(D.2)

Applying Jacobi's law on the term on *LHS* and recognizing from the property of trace that $\text{Tr}(\mu \ell^T) = \text{Tr}(\ell) = \frac{j}{J}$ we can write:

$$2\frac{\dot{J}_{e}}{J_{e}} = 2\frac{\dot{J}}{J} - 2k_{T} + k_{T} \operatorname{Tr}(\mu_{T}\mu^{-1}) \quad \text{where} \quad \frac{\dot{J}}{J} = \frac{\dot{J}_{e}}{J_{e}} + \frac{\dot{\eta}}{\eta} + \frac{\dot{\zeta}_{i}}{\zeta_{i}}$$
 (D.3)

Now using the conditions of T1 transitions: $\dot{\eta}/\eta = 0$ and $\dot{\zeta}_i/\zeta_i = 0$, we get $\dot{J}/J = \dot{J}_e/J_e$ which when substituted in eqn. (D.3) results in the required constrained condition on μ_T as:

$$\operatorname{Tr}(\mu_T \mu^{-1}) = 2 \tag{D.4}$$

which can then be used to find out μ_T using $\mu_T = \mu_T I$.

Appendix D.2. Dissipation \mathcal{D}_T

Considering T1 transition is the only inelastic mechanism operating, we have: $\dot{\psi}_i = (\partial \psi_i / \partial \mu) : \dot{\mu}$ and $\dot{\rho}_i / \rho_i = 0$. Now using these conditions and $\mathcal{L}(\mu) = -d_T$ in Clausius-Duhem inequality (3.27), we get:

$$\mathscr{D} = \left(\sigma - \frac{2}{J_e} \frac{\partial \psi_i}{\partial \mu} \mu\right) : \ell + \underbrace{\frac{1}{J_e} \frac{\partial \psi_i}{\partial \mu} : d_T}_{\mathscr{D}_T} \ge 0 \tag{D.5}$$

where the first term is the elastic term and vanishes whereas the second term models dissipation \mathcal{D}_T due to T1 transitions. From this, we can write:

$$\mathscr{D}_T = \frac{1}{J_e} \frac{\partial \psi_i}{\partial \mu} : d_T \tag{D.6}$$

$$\mathscr{D}_T = \frac{1}{J_e} \operatorname{Tr} \left(\frac{\partial \psi_i}{\partial \mu} d_T^T \right) \tag{D.7}$$

Using eqn. (C.4) and identifying d_T is symmetric, we can write:

$$\mathscr{D}_T = \frac{1}{J_e} \operatorname{Tr} \left[\left(\frac{\partial \psi_i}{\partial I_1} \mathbf{I} + \frac{\partial \psi_i}{\partial I_3} I_3 \boldsymbol{\mu}^{-1} \right) \boldsymbol{d}_T \right]$$
 (D.8)

$$\mathscr{D}_{T} = \frac{1}{J_{e}} \left[\frac{\partial \psi_{i}}{\partial I_{1}} \operatorname{Tr}(\boldsymbol{d}_{T}) + \frac{\partial \psi_{i}}{\partial I_{3}} I_{3} \operatorname{Tr}(\boldsymbol{\mu}^{-1} \boldsymbol{d}_{T}) \right]$$
(D.9)

Substituting d_T from eqn. (5.6) in above, we finally get:

$$\mathscr{D}_T = \frac{k_T}{J_e} \frac{\partial \psi_i}{\partial I_1} \operatorname{Tr} \left(\mu - \frac{2}{\operatorname{Tr}(\mu^{-1})} \mathbf{I} \right) \tag{D.10}$$

Appendix D.3. Numerical solution for example 5.1.1a.

Let the superscript n denote the value of the variable at n_{th} time step. To determine the ℓ_2^{n-1} and $\mu^n = diag[\mu_1^n \mu_2^n]$, we first employ a first-order forward-Euler integration scheme to obtain:

$$\mu^{n} = \mu^{n-1} + \dot{\mu}^{n-1} \Delta t \tag{D.11}$$

where $\mu^{n-1} = diag[\mu_1^{n-1} \ \mu_2^{n-1}]$ is known from previous time step and Δt is the time increment. Next, we calculate the current stress tensor $\sigma^n = diag[\sigma_1^n \ \sigma_2^n]$ using eqn. (4.6) and then set $\sigma_2^n = 0$, which allows the tissue to deform freely transversely. This yields a non-linear system of three equations in three variables $(\ell_2^{n-1}, \mu_1^n, \mu_2^n)$ given by:

$$\begin{bmatrix} \frac{\zeta_{0}}{2} \left(\zeta_{0} \sqrt{\mu_{1}^{n} \mu_{2}^{n}} - 1 \right) + \frac{\bar{\Gamma}_{p_{p}}}{\sqrt{\mu_{1}^{n} \mu_{2}^{n}}} \left(\frac{\pi \zeta_{0}}{p_{p}} - \sqrt{\frac{\pi \zeta_{0}}{2(\mu_{1}^{n} + \mu_{2}^{n})}} \right) \mu_{2}^{n} \\ \mu_{1}^{n} - \mu_{1}^{n-1} \left(2\ell_{1}^{n-1} - k_{T}^{n-1} \left(\frac{\mu_{1}^{n-1} - \mu_{2}^{n-1}}{\mu_{1}^{n-1} + \mu_{2}^{n-1}} \right) \right) \Delta t - \mu_{1}^{n-1} \\ \mu_{2}^{n} - \mu_{2}^{n-1} \left(2\ell_{2}^{n-1} + k_{T}^{n-1} \left(\frac{\mu_{1}^{n-1} - \mu_{2}^{n-1}}{\mu_{1}^{n-1} + \mu_{2}^{n-1}} \right) \right) \Delta t - \mu_{2}^{n-1} \end{bmatrix} = \begin{bmatrix} 0 \\ 0 \\ 0 \end{bmatrix}$$
(D.12)

Having solved for these unknowns, we can then update the remaining quantities such as σ_1^n and deformation gradient $\mathbf{F}^n = diag[\lambda_1^n \ \lambda_2^n]$ accordingly.

Appendix E. Derivations for cell division

Appendix E.1. Cell division flow rate

Recall that;

$$\mathscr{L}(\boldsymbol{\mu}) = -\frac{\dot{\zeta}_{l}}{\zeta_{l}}\boldsymbol{\mu} - \frac{2\pi}{z}\frac{1}{J_{l}}\left[\int_{\Omega} (\xi_{l} - p\Xi_{l})\boldsymbol{r}\otimes\boldsymbol{r}\,d\Omega - \int_{\Omega} (\xi_{c} - p\Xi_{c})\boldsymbol{r}\otimes\boldsymbol{r}\,d\Omega\right]$$
(E.1)

Considering no other inelastic mechanism and substituting eqns. (5.14) and (5.16) in eqn. (E.1) we get:

$$\mathcal{L}(\boldsymbol{\mu}) = -k_D \boldsymbol{\mu} + 2k_D \boldsymbol{\mu}_D \implies \boldsymbol{d}_D = k_D (\boldsymbol{\mu} - 2\boldsymbol{\mu}_D)$$
 (E.2)

Using this d_D we can write the evolution equation for μ pertaining to cell division as:

$$\dot{\boldsymbol{\mu}} = \boldsymbol{\ell} \boldsymbol{\mu} + \boldsymbol{\mu} \boldsymbol{\ell}^T - k_D (\boldsymbol{\mu} - 2\boldsymbol{\mu}_D) \tag{E.3}$$

Just like we did for T1 transitions, multiply by μ^{-1} and take the trace to finally obtain:

$$2\frac{\dot{J}_e}{J_e} = 2\frac{\dot{J}}{J} - 2k_D + 2k_D \operatorname{Tr}(\mu_D \mu^{-1}) \quad \text{where} \quad \frac{\dot{J}}{J} = \frac{\dot{J}_e}{J_e} + \frac{\dot{\eta}}{\eta} + \frac{\dot{\zeta}_i}{\zeta_i}$$
 (E.4)

Now using the cell division conditions: $\dot{\eta}/\eta = k_D$ and $\dot{\zeta}_i/\zeta_i = -k_D$, the constrained condition on μ_D becomes:

$$\operatorname{Tr}(\mu_D \mu^{-1}) = 1 \tag{E.5}$$

which then can be used to derive μ_D for different cases depending on the biased or random nature of cell division.

Appendix E.2. Dissipation \mathcal{D}_D

To derive \mathcal{D}_D , which is mechanical dissipation due to passive cell divisions, we will follow the same steps as we did for T1 transitions in Appendix D.2.

First we find $\dot{\psi}_i$ which now also includes the contribution from ISV ζ_i as:

$$\dot{\psi}_i = \frac{\partial \psi_i}{\partial \boldsymbol{\mu}} : \dot{\boldsymbol{\mu}} + \frac{\dot{\zeta}_i}{\zeta_i} \psi_i \tag{E.6}$$

We can show then when cell division is the only inelastic process, then $\dot{\rho}_i/\rho_i = 0$. Suppose the mass of the system is, say given by, \mathcal{M} . ρ_i , in that case, is defined as:

$$\rho_i = \frac{\mathcal{M}}{a_i} = \frac{\mathcal{M}}{J_i a(0)} = \frac{\mathcal{M}}{\eta \zeta_i a(0)} \tag{E.7}$$

The material time derivative of ρ_i , using chain rule becomes:

$$\frac{\dot{\rho}_i}{\rho_i} = \frac{\dot{\mathcal{M}}}{\mathcal{M}} - \frac{\dot{J}_i}{J_i} = \frac{\dot{\mathcal{M}}}{\mathcal{M}} - \left(\frac{\dot{\eta}}{\eta} + \frac{\dot{\zeta}_i}{\zeta_i}\right) \tag{E.8}$$

In the absence of tissue growth: $\dot{\mathcal{M}} = 0$. Also using condition from cell division: $\frac{\dot{J}_i}{J_i} = \frac{\dot{\eta}}{\eta} + \frac{\dot{\xi}_i}{\zeta_i} = 0$, the mass density ρ_i in intermediate configuration remains unchanged. Now using this condition and $\mathcal{L}(\mu) = -d_D$ in Clausius-Duhem inequality (3.27), we get:

$$\mathscr{D} = \left(\sigma - \frac{2}{J_e} \frac{\partial \psi_i}{\partial \mu} \mu\right) : \ell + \underbrace{\frac{1}{J_e} \frac{\partial \psi_i}{\partial \mu} : d_T - \frac{1}{J_e} \frac{\dot{\zeta}_i}{\zeta_i} \psi_i}_{\mathscr{D}_D} \ge 0$$
(E.9)

where again the first term vanishes whereas the second and third terms combine to model the dissipation \mathcal{D}_D due to the passive cell divisions. Substituting d_D from eqn. (E.2), we finally get:

$$\mathscr{D}_D = \frac{k_D}{J_e} \frac{\partial \psi_i}{\partial I_1} \operatorname{Tr} \left(\mu - \frac{2}{\operatorname{Tr}(\mu^{-1})} \mathbf{I} \right) - \frac{1}{J_e} \frac{\dot{\zeta}_i}{\zeta_i} \psi_i \quad \text{where recall that} \quad \frac{\dot{\zeta}_i}{\zeta_i} = -k_D$$
 (E.10)

References

Silvanus Alt, Poulami Ganguly, and Guillaume Salbreux. Vertex models: from cell mechanics to tissue morphogenesis. *Philosophical Transactions of the Royal Society B: Biological Sciences*, 372(1720):20150520, May 2017. ISSN 0962-8436, 1471-2970. doi: 10.1098/rstb.2015.0520. URL https://royalsocietypublishing.org/doi/10.1098/rstb.2015.0520

D. Ambrosi and F. Mollica. The role of stress in the growth of a multicell spheroid. *Journal of Mathematical Biology*, 48(5):477–499, May 2004. ISSN 0303-6812, 1432-1416. doi: 10.1007/s00285-003-0238-2. URL http://link.springer.com/10.1007/s00285-003-0238-2.

Atef Asnacios and Olivier Hamant. The mechanics behind cell polarity. Trends in Cell Biology, 22(11):584-591, November 2012. ISSN 09628924. doi: 10.1016/j.tcb.2012.08.005. URL https://linkinghub.elsevier.com/retrieve/pii/S0962892412001444

Daniel L. Barton, Silke Henkes, Cornelis J. Weijer, and Rastko Sknepnek. Active Vertex Model for cell-resolution description of epithelial tissue mechanics. *PLOS Computational Biology*, 13(6):e1005569, June 2017. ISSN 1553-7358. doi: 10.1371/journal.pcbi.1005569. URL https://dx.plos.org/10.1371/journal.pcbi.1005569.

Claire Bertet, Lawrence Sulak, and Thomas Lecuit. Myosin-dependent junction remodelling controls planar cell intercalation and axis elongation. *Nature*, 429(6992):667-671, June 2004. ISSN 0028-0836, 1476-4687. doi: 10.1038/nature02590. URL http://www.nature.com/articles/nature02590

Dapeng Bi, Jorge H. Lopez, J. M. Schwarz, and M. Lisa Manning. Energy barriers and cell migration in densely packed tissues. *Soft Matter*, 10 (12):1885, 2014. ISSN 1744-683X, 1744-6848. doi: 10.1039/c3sm52893f. URL http://xlink.rsc.org/?DOI=c3sm52893f

Dapeng Bi, J. H. Lopez, J. M. Schwarz, and M. Lisa Manning. A density-independent rigidity transition in biological tissues. *Nature Physics*, 11(12):1074-1079, December 2015. ISSN 1745-2473, 1745-2481. doi: 10.1038/nphys3471. URL http://www.nature.com/articles/nphys3471.

Dapeng Bi, Xingbo Yang, M. Cristina Marchetti, and M. Lisa Manning. Motility-Driven Glass and Jamming Transitions in Biological Tissues. Physical Review X, 6(2):021011, April 2016. ISSN 2160-3308. doi: 10.1103/PhysRevX.6.021011. URL https://link.aps.org/doi/10.1103/PhysRevX.6.021011.

- Guy B Blanchard, Alexandre J Kabla, Nora L Schultz, Lucy C Butler, Benedicte Sanson, Nicole Gorfinkiel, L Mahadevan, and Richard J Adams. Tissue tectonics: morphogenetic strain rates, cell shape change and intercalation. *Nature Methods*, 6(6):458–464, June 2009. ISSN 1548-7091, 1548-7105. doi: 10.1038/nmeth.1327. URL https://www.nature.com/articles/nmeth.1327.
- Martin Bock, Amit Kumar Tyagi, Jan-Ulrich Kreft, and Wolfgang Alt. Generalized Voronoi Tessellation as a Model of Two-dimensional Cell Tissue Dynamics. *Bulletin of Mathematical Biology*, 72(7):1696–1731, October 2010. ISSN 0092-8240, 1522-9602. doi: 10.1007/s11538-009-9498-3. URL http://link.springer.com/10.1007/s11538-009-9498-3.
- G Brodland, D Chen, and J Veldhuis. A cell-based constitutive model for embryonic epithelia and other planar aggregates of biological cells. *International Journal of Plasticity*, 22(6):965–995, June 2006. ISSN 07496419. doi: 10.1016/j.ijplas.2005.05.002. URL https://linkinghub.elsevier.com/retrieve/pii/S0749641905000999
- Lucy C. Butler, Guy B. Blanchard, Alexandre J. Kabla, Nicola J. Lawrence, David P. Welchman, L. Mahadevan, Richard J. Adams, and Benedicte Sanson. Cell shape changes indicate a role for extrinsic tensile forces in Drosophila germ-band extension. *Nature Cell Biology*, 11(7):859–864, July 2009. ISSN 1465-7392, 1476-4679. doi: 10.1038/ncb1894. URL http://www.nature.com/articles/ncb1894
- Raphaël Clément, Benoît Dehapiot, Claudio Collinet, Thomas Lecuit, and Pierre-François Lenne. Viscoelastic Dissipation Stabilizes Cell Shape Changes during Tissue Morphogenesis. *Current Biology*, 27(20):3132–3142.e4, October 2017. ISSN 09609822. doi: 10.1016/j.cub.2017.09. 005. URL https://linkinghub.elsevier.com/retrieve/pii/S0960982217311697
- P. Coussot. Yield stress fluid flows: A review of experimental data. *Journal of Non-Newtonian Fluid Mechanics*, 211:31-49, September 2014. ISSN 03770257. doi: 10.1016/j.jnnfm.2014.05.006. URL https://linkinghub.elsevier.com/retrieve/pii/S0377025714000895
- Amin Doostmohammadi, Sumesh P. Thampi, Thuan B. Saw, Chwee T. Lim, Benoit Ladoux, and Julia M. Yeomans. Cell division: a source of active stress in cellular monolayers. *Soft Matter*, 11(37):7328–7336, 2015. ISSN 1744-683X, 1744-6848. doi: 10.1039/C5SM01382H. URL http://arxiv.org/abs/1508.01408 arXiv:1508.01408 [cond-mat, physics:physics].
- Yangkun Du, Chaofeng Lü, Weiqiu Chen, and Michel Destrade. Modified multiplicative decomposition model for tissue growth: Beyond the initial stress-free state. *Journal of the Mechanics and Physics of Solids*, 118:133–151, September 2018. ISSN 00225096. doi: 10.1016/j.jmps.2018. 05.014. URL http://arxiv.org/abs/2009.01738 arXiv:2009.01738 [cond-mat, physics:nlin].
- Charlie Duclut, Joris Paijmans, Mandar M. Inamdar, Carl D. Modes, and Frank Jülicher. Nonlinear rheology of cellular networks. Cells & Development, 168:203746, December 2021. ISSN 26672901. doi: 10.1016/j.cdev.2021.203746. URL https://linkinghub.elsevier.com/retrieve/pii/S2667290121000802
- Charlie Duclut, Joris Paijmans, Mandar M. Inamdar, Carl D. Modes, and Frank Jülicher. Active T1 transitions in cellular networks, March 2022. URL http://arxiv.org/abs/2111.10327 arXiv:2111.10327 [cond-mat, physics:physics].
- Gonca Erdemci-Tandogan and M. Lisa Manning. Effect of cellular rearrangement time delays on the rheology of vertex models for confluent tissues. *PLOS Computational Biology*, 17(6):e1009049, June 2021. ISSN 1553-7358. doi: 10.1371/journal.pcbi.1009049. URL https://dx.plos.org/10.1371/journal.pcbi.1009049.
- Henry Eyring. Viscosity, Plasticity, and Diffusion as Examples of Absolute Reaction Rates. *The Journal of Chemical Physics*, 4(4):283–291, April 1936. ISSN 0021-9606, 1089-7690. doi: 10.1063/1.1749836. URL https://pubs.aip.org/aip/jcp/article/4/4/283-291/207491
- Reza Farhadifar, Jens-Christian Röper, Benoit Aigouy, Suzanne Eaton, and Frank Jülicher. The Influence of Cell Mechanics, Cell-Cell Interactions, and Proliferation on Epithelial Packing. Current Biology, 17(24):2095–2104, December 2007. ISSN 09609822. doi: 10.1016/j.cub.2007.11.049. URL https://linkinghub.elsevier.com/retrieve/pii/S0960982207023342
- Rodrigo Fernandez-Gonzalez, Sérgio de Matos Simoes, Jens-Christian Röper, Suzanne Eaton, and Jennifer A. Zallen. Myosin II Dynamics Are Regulated by Tension in Intercalating Cells. *Developmental Cell*, 17(5):736–743, November 2009. ISSN 15345807. doi: 10.1016/j.devcel. 2009.09.003. URL https://linkinghub.elsevier.com/retrieve/pii/S1534580709003852
- Alexander G. Fletcher, James M. Osborne, Philip K. Maini, and David J. Gavaghan. Implementing vertex dynamics models of cell populations in biology within a consistent computational framework. *Progress in Biophysics and Molecular Biology*, 113(2):299–326, November 2013. ISSN 00796107. doi: 10.1016/j.pbiomolbio.2013.09.003. URL https://linkinghub.elsevier.com/retrieve/pii/S0079610713000989
- Alexander G. Fletcher, Fergus Cooper, and Ruth E. Baker. Mechanocellular models of epithelial morphogenesis. *Philosophical Transactions of the Royal Society B: Biological Sciences*, 372(1720):20150519, May 2017. ISSN 0962-8436, 1471-2970. doi: 10.1098/rstb.2015.0519. URL https://royalsocietypublishing.org/doi/10.1098/rstb.2015.0519
- Alexander G. Fletcher, Miriam Osterfield, Ruth E. Baker, and Stanislav Y. Shvartsman. Vertex Models of Epithelial Morphogenesis. *Biophysical Journal*, 106(11):2291-2304, June 2014. ISSN 00063495. doi: 10.1016/j.bpj.2013.11.4498. URL https://linkinghub.elsevier.com/retrieve/pii/S0006349513057949
- Paul J. Flory and John Rehner. Statistical Mechanics of Cross-Linked Polymer Networks I. Rubberlike Elasticity. *The Journal of Chemical Physics*, 11(11):512–520, November 1943. ISSN 0021-9606, 1089-7690. doi: 10.1063/1.1723791. URL http://aip.scitation.org/doi/10.1063/1.1723791
- Peter Friedl and Darren Gilmour. Collective cell migration in morphogenesis, regeneration and cancer. Nature Reviews Molecular Cell Biology, 10(7):445–457, July 2009. ISSN 1471-0072, 1471-0080. doi: 10.1038/nrm2720. URL http://www.nature.com/articles/nrm2720
- K. Garikipati. The Kinematics of Biological Growth. Applied Mechanics Reviews, 62(3):030801, May 2009. ISSN 0003-6900, 2379-0407. doi: 10.1115/1.3090829. URL https://asmedigitalcollection.asme.org/appliedmechanicsreviews/article/doi/10.1115/1.3090829/443740/The-Kinematics-of-Biological-Growth
- M. Genet. A relaxed growth modeling framework for controlling growth-induced residual stresses. Clinical Biomechanics, 70:270-277, December 2019. ISSN 02680033. doi: 10.1016/j.clinbiomech.2019.08.015. URL https://linkinghub.elsevier.com/retrieve/pii/S0268003319301305.
- Nikolce Gjorevski and Celeste M. Nelson. The mechanics of development: Models and methods for tissue morphogenesis. Birth Defects Research Part C: Embryo Today: Reviews, 90(3):193–202, September 2010. ISSN 1542975X. doi: 10.1002/bdrc.20185. URL https://onlinelibrary.wiley.com/doi/10.1002/bdrc.20185
- Alain Goriely. The Mathematics and Mechanics of Biological Growth, volume 45 of Interdisciplinary Applied Mathematics. Springer New York, New York, NY, 2017. ISBN 978-0-387-87709-9 978-0-387-87710-5. doi: 10.1007/978-0-387-87710-5. URL http://link.springer.com/10.1007/978-0-387-87710-5.

- François Graner, B. Dollet, Christophe Raufaste, and Philippe Marmottant. Discrete rearranging disordered patterns, part I: Robust statistical tools in two or three dimensions. *The European Physical Journal E*, 25(4):349–369, April 2008. ISSN 1292-8941, 1292-895X. doi: 10.1140/epje/i2007-10298-8. URL http://arxiv.org/abs/0708.3193 arXiv:0708.3193 [cond-mat].
- Boris Guirao, Stéphane U Rigaud, Floris Bosveld, Anaïs Bailles, Jesús López-Gay, Shuji Ishihara, Kaoru Sugimura, François Graner, and Yohanns Bellaïche. Unified quantitative characterization of epithelial tissue development. *eLife*, 4:e08519, December 2015. ISSN 2050-084X. doi: 10.7554/eLife.08519. URL https://elifesciences.org/articles/08519
- Andrew R. Harris, Loic Peter, Julien Bellis, Buzz Baum, Alexandre J. Kabla, and Guillaume T. Charras. Characterizing the mechanics of cultured cell monolayers. *Proceedings of the National Academy of Sciences*, 109(41):16449–16454, October 2012. ISSN 0027-8424, 1091-6490. doi: 10.1073/pnas.1213301109. URL https://pnas.org/doi/full/10.1073/pnas.1213301109
- Carl-Philipp Heisenberg and Yohanns Bellaïche. Forces in Tissue Morphogenesis and Patterning. Cell, 153(5):948-962, May 2013. ISSN 00928674. doi: 10.1016/j.cell.2013.05.008. URL https://linkinghub.elsevier.com/retrieve/pii/S0092867413005734
- Gabriel Helmlinger, Paolo A Netti, Hera C Lichtenbeld, Robert J Melder, and Rakesh K Jain. Solid stress inhibits the growth of 1nulticellular tu1nor spheroids. *Nature Biotechnology*, 15:6, 1997. doi: 10.1038/nbt0897-778.
- A. Hoger, T. J. Van Dyke, and V. A. Lubarda. Symmetrization of the growth deformation and velocity gradients in residually stressed biomaterials. Zeitschrift f r angewandte Mathematik und Physik, 55(5):848–860, September 2004. ISSN 0044-2275, 1420-9039. doi: 10.1007/s00033-004-3029-8. URL http://link.springer.com/10.1007/s00033-004-3029-8.
- Ruoyu Huang, Raymond W. Ogden, and Raimondo Penta. Mathematical Modelling of Residual-Stress Based Volumetric Growth in Soft Matter. Journal of Elasticity, 145(1-2):223-241, August 2021. ISSN 0374-3535, 1573-2681. doi: 10.1007/s10659-021-09834-8. URL https://link.springer.com/10.1007/s10659-021-09834-8
- J. D. Humphrey. Constrained Mixture Models of Soft Tissue Growth and Remodeling Twenty Years After. *Journal of Elasticity*, 145(1-2): 49-75, August 2021. ISSN 0374-3535, 1573-2681. doi: 10.1007/s10659-020-09809-1. URL https://link.springer.com/10.1007/s10659-020-09809-1
- Shuji Ishihara, Philippe Marcq, and Kaoru Sugimura. From cells to tissue: A continuum model of epithelial mechanics. *Physical Review E*, 96 (2):022418, August 2017. ISSN 2470-0045, 2470-0053. doi: 10.1103/PhysRevE.96.022418. URL https://link.aps.org/doi/10.1103/PhysRevE.96.022418.
- Andreas Janshoff. Viscoelastic properties of epithelial cells. *Biochemical Society Transactions*, 49(6):2687-2695, December 2021. ISSN 0300-5127, 1470-8752. doi: 10.1042/BST20210476. URL https://portlandpress.com/biochemsoctrans/article/49/6/2687/230361/Viscoelastic-properties-of-epithelial-cells.
- Gareth Wyn Jones and S. Jonathan Chapman. Modeling Growth in Biological Materials. SIAM Review, 54(1):52–118, 2012. doi: 10.1137/080731785. URL https://doi.org/10.1137/080731785. eprint: https://doi.org/10.1137/080731785.
- Sangwoo Kim, Marie Pochitaloff, Georgina A. Stooke-Vaughan, and Otger Campàs. Embryonic tissues as active foams. Nature Physics, 17 (7):859-866, July 2021. ISSN 1745-2473, 1745-2481. doi: 10.1038/s41567-021-01215-1. URL http://www.nature.com/articles/s41567-021-01215-1
- Deqing Kong, Fred Wolf, and Jörg Großhans. Forces directing germ-band extension in Drosophila embryos. *Mechanisms of Development*, 144:11-22, April 2017. ISSN 09254773. doi: 10.1016/j.mod.2016.12.001. URL https://linkinghub.elsevier.com/retrieve/pii/S0925477316300971
- Matej Krajnc, Sabyasachi Dasgupta, Primož Ziherl, and Jacques Prost. Fluidization of epithelial sheets by active cell rearrangements. *Physical Review E*, 98(2):022409, August 2018. ISSN 2470-0045, 2470-0053. doi: 10.1103/PhysRevE.98.022409. URL https://link.aps.org/doi/10.1103/PhysRevE.98.022409.
- Jonathan Kulwatno, Jamie Gearhart, Xiangyu Gong, Nora Herzog, Matthew Getzin, Mihaela Skobe, and Kristen L Mills. Growth of tumor emboli within a vessel model reveals dependence on the magnitude of mechanical constraint. *Integrative Biology*, 13(1):1–16, February 2021. ISSN 1757-9708. doi: 10.1093/intbio/zyaa024. URL https://academic.oup.com/ib/article/13/1/1/6092822
- Raz Kupferman, Ben Maman, and Michael Moshe. Continuum mechanics of a cellular tissue model. *Journal of the Mechanics and Physics of Solids*, 143:104085, October 2020. ISSN 00225096. doi: 10.1016/j.jmps.2020.104085. URL https://linkinghub.elsevier.com/retrieve/pii/S0022509620303197
- Jos Käfer, Takashi Hayashi, Athanasius F. M. Marée, Richard W. Carthew, and François Graner. Cell adhesion and cortex contractility determine cell patterning in the *Drosophila* retina. *Proceedings of the National Academy of Sciences*, 104(47):18549–18554, November 2007. ISSN 0027-8424, 1091-6490. doi: 10.1073/pnas.0704235104. URL https://pnas.org/doi/full/10.1073/pnas.0704235104
- Benoit Ladoux and René-Marc Mège. Mechanobiology of collective cell behaviours. *Nature Reviews Molecular Cell Biology*, 18(12):743-757, December 2017. ISSN 1471-0072, 1471-0080. doi: 10.1038/nrm.2017.98. URL http://www.nature.com/articles/nrm.2017.98
- Thomas Lecuit and Pierre-François Lenne. Cell surface mechanics and the control of cell shape, tissue patterns and morphogenesis. *Nature Reviews Molecular Cell Biology*, 8(8):633–644, August 2007. ISSN 1471-0072, 1471-0080. doi: 10.1038/nrm2222. URL http://www.nature.com/articles/nrm2222
- E. H. Lee. Elastic-Plastic Deformation at Finite Strains. *Journal of Applied Mechanics*, 36(1):1–6, March 1969. ISSN 0021-8936. doi: 10. 1115/1.3564580. URL https://doi.org/10.1115/1.3564580 eprint: https://asmedigitalcollection.asme.org/appliedmechanics/article-pdf/36/1/1/5449476/1_1.pdf.
- Shao-Zhen Lin, Bo Li, and Xi-Qiao Feng. A dynamic cellular vertex model of growing epithelial tissues. *Acta Mechanica Sinica*, 33(2): 250-259, April 2017. ISSN 0567-7718, 1614-3116. doi: 10.1007/s10409-017-0654-y. URL http://link.springer.com/10.1007/s10409-017-0654-y.
- V.A. Lubarda and A. Hoger. On the mechanics of solids with a growing mass. International Journal of Solids and Structures, 39(18):4627–4664, September 2002. ISSN 00207683. doi: 10.1016/S0020-7683(02)00352-9. URL https://linkinghub.elsevier.com/retrieve/pii/S0020768302003529.
- Philippe Marmottant, Abbas Mgharbel, Jos Käfer, Benjamin Audren, Jean-Paul Rieu, Jean-Claude Vial, Boudewijn van der Sanden, Athanasius F. M. Marée, François Graner, and Hélène Delanoë-Ayari. The role of fluctuations and stress on the effective viscosity of cell aggregates. *Proceedings of the National Academy of Sciences*, 106(41):17271–17275, October 2009. ISSN 0027-8424, 1091-6490. doi: 10.1073/pnas.

- 0902085106. URL https://pnas.org/doi/full/10.1073/pnas.0902085106.
- D. A. Matoz-Fernandez, Elisabeth Agoritsas, Jean-Louis Barrat, Eric Bertin, and Kirsten Martens. Nonlinear Rheology in a Model Biological Tissue. *Physical Review Letters*, 118(15):158105, April 2017. ISSN 0031-9007, 1079-7114. doi: 10.1103/PhysRevLett.118.158105. URL http://link.aps.org/doi/10.1103/PhysRevLett.118.158105
- Aziza Merzouki, Orestis Malaspinas, and Bastien Chopard. The mechanical properties of a cell-based numerical model of epithelium. *Soft Matter*, 12(21):4745–4754, 2016. ISSN 1744-683X, 1744-6848. doi: 10.1039/C6SM00106H. URL http://xlink.rsc.org/?D0I=C6SM00106H.
- Denise J. Montell. Morphogenetic Cell Movements: Diversity from Modular Mechanical Properties. Science, 322(5907):1502-1505, December 2008. ISSN 0036-8075, 1095-9203. doi: 10.1126/science.1164073. URL https://www.science.org/doi/10.1126/science.1164073.
- James M. Osborne, Alexander G. Fletcher, Joe M. Pitt-Francis, Philip K. Maini, and David J. Gavaghan. Comparing individual-based approaches to modelling the self-organization of multicellular tissues. *PLOS Computational Biology*, 13(2):e1005387, February 2017. ISSN 1553-7358. doi: 10.1371/journal.pcbi.1005387. URL https://dx.plos.org/10.1371/journal.pcbi.1005387.
- Linda Oswald, Steffen Grosser, David M Smith, and Josef A Käs. Jamming transitions in cancer. *Journal of Physics D: Applied Physics*, 50(48): 483001, December 2017. ISSN 0022-3727, 1361-6463. doi: 10.1088/1361-6463/aa8e83. URL https://iopscience.iop.org/article/10.1088/1361-6463/aa8e83.
- Marko Popović, Amitabha Nandi, Matthias Merkel, Raphaël Etournay, Suzanne Eaton, Frank Jülicher, and Guillaume Salbreux. Active dynamics of tissue shear flow. New Journal of Physics, 19(3):033006, March 2017. ISSN 1367-2630. doi: 10.1088/1367-2630/aa5756. URL https://iopscience.iop.org/article/10.1088/1367-2630/aa5756
- L. Preziosi, D. Ambrosi, and C. Verdier. An elasto-visco-plastic model of cell aggregates. Journal of Theoretical Biology, 262(1):35–47, January 2010. ISSN 00225193. doi: 10.1016/j.jtbi.2009.08.023. URL https://linkinghub.elsevier.com/retrieve/pii/S0022519309003841
- Matteo Rauzi, Pascale Verant, Thomas Lecuit, and Pierre-François Lenne. Nature and anisotropy of cortical forces orienting Drosophila tissue morphogenesis. *Nature Cell Biology*, 10(12):1401–1410, December 2008. ISSN 1465-7392, 1476-4679. doi: 10.1038/ncb1798. URL http://www.nature.com/articles/ncb1798
- Edward K. Rodriguez, Anne Hoger, and Andrew D. McCulloch. Stress-dependent finite growth in soft elastic tissues. *Journal of Biomechanics*, 27 (4):455-467, April 1994. ISSN 00219290. doi: 10.1016/0021-9290(94)90021-3. URL https://linkinghub.elsevier.com/retrieve/pii/0021929094900213
- Daria S. Roshal, Marianne Martin, Kirill Fedorenko, Ivan Golushko, Virginie Molle, Stephen Baghdiguian, and Sergei B. Rochal. Random nature of epithelial cancer cell monolayers. *Journal of The Royal Society Interface*, 19(190):20220026, May 2022. ISSN 1742-5662. doi: 10.1098/rsif.2022.0026. URL https://royalsocietypublishing.org/doi/10.1098/rsif.2022.0026
- Giuliana Rossi, Andrea Manfrin, and Matthias P. Lutolf. Progress and potential in organoid research. *Nature Reviews Genetics*, 19(11):671–687, November 2018. ISSN 1471-0056, 1471-0064. doi: 10.1038/s41576-018-0051-9. URL https://www.nature.com/articles/s41576-018-0051-9
- Jan Rozman, Matej Krajnc, and Primož Ziherl. Collective cell mechanics of epithelial shells with organoid-like morphologies. *Nature Communications*, 11(1):3805, December 2020. ISSN 2041-1723. doi: 10.1038/s41467-020-17535-4. URL http://www.nature.com/articles/s41467-020-17535-4
- Monirosadat Sadati, Nader Taheri Qazvini, Ramaswamy Krishnan, Chan Young Park, and Jeffrey J. Fredberg. Collective migration and cell jamming. *Differentiation*, 86(3):121-125, October 2013. ISSN 03014681. doi: 10.1016/j.diff.2013.02.005. URL https://linkinghub.elsevier.com/retrieve/pii/S0301468113000170
- Eva-Maria Schötz, Marcos Lanio, Jared A. Talbot, and M. Lisa Manning. Glassy dynamics in three-dimensional embryonic tissues. *Journal of The Royal Society Interface*, 10(89):20130726, December 2013. ISSN 1742-5689, 1742-5662. doi: 10.1098/rsif.2013.0726. URL https://royalsocietypublishing.org/doi/10.1098/rsif.2013.0726
- Richard Skalak, Stephen Zargaryan, Rakesh K Jain, Paolo A Netti, and Anne Hoger. Compatibility and the genesis of residual stress by volumetric growth. *Journal of Mathematical Biology*, page 26, 1996. doi: 10.1007/BF01834825.
- Michael F. Staddon, Arthur Hernandez, Mark J. Bowick, Michael Moshe, and M. Cristina Marchetti. The role of non-affine deformations in the elastic behavior of the cellular vertex model. *Soft Matter*, page 10.1039.D2SM01580C, 2023. ISSN 1744-683X, 1744-6848. doi: 10.1039/D2SM01580C. URL http://arxiv.org/abs/2211.17020 arXiv:2211.17020 [cond-mat, physics:physics].
- D. B. Staple, R. Farhadifar, J. C. Röper, B. Aigouy, S. Eaton, and F. Jülicher. Mechanics and remodelling of cell packings in epithelia. *The European Physical Journal E*, 33(2):117–127, October 2010. ISSN 1292-8941, 1292-895X. doi: 10.1140/epje/i2010-10677-0. URL http://link.springer.com/10.1140/epje/i2010-10677-0
- András Szabó and Roeland M. H. Merks. Cellular Potts Modeling of Tumor Growth, Tumor Invasion, and Tumor Evolution. Frontiers in Oncology, 3, 2013. ISSN 2234-943X. doi: 10.3389/fonc.2013.00087. URL http://journal.frontiersin.org/article/10.3389/fonc.2013.00087/abstract
- F. Tanaka and S. F. Edwards. Viscoelastic properties of physically crosslinked networks. 1. Transient network theory. *Macromolecules*, 25(5): 1516-1523, March 1992. ISSN 0024-9297, 1520-5835. doi: 10.1021/ma00031a024. URL https://pubs.acs.org/doi/abs/10.1021/ma00031a024
- Robert J. Tetley and Yanlan Mao. The same but different: cell intercalation as a driver of tissue deformation and fluidity. *Philosophical Transactions of the Royal Society B: Biological Sciences*, 373(1759):20170328, November 2018. ISSN 0962-8436, 1471-2970. doi: 10.1098/rstb.2017.0328. URL https://royalsocietypublishing.org/doi/10.1098/rstb.2017.0328
- Robert J. Tetley, Michael F. Staddon, Davide Heller, Andreas Hoppe, Shiladitya Banerjee, and Yanlan Mao. Tissue fluidity promotes epithelial wound healing. *Nature Physics*, 15(11):1195–1203, November 2019. ISSN 1745-2473, 1745-2481. doi: 10.1038/s41567-019-0618-1. URL https://www.nature.com/articles/s41567-019-0618-1.
- Sham Tilil, Cyprien Gay, François Graner, Philippe Marcq, François Molino, and Pierre Saramito. Colloquium: Mechanical formalisms for tissue dynamics. *The European Physical Journal E*, 38(5):33, May 2015. ISSN 1292-8941, 1292-895X. doi: 10.1140/epje/i2015-15033-4. URL http://link.springer.com/10.1140/epje/i2015-15033-4.
- Sijie Tong, Navreeta K. Singh, Rastko Sknepnek, and Andrej Kosmrlj. Linear Viscoelastic Properties of the Vertex Model for Epithelial Tissues,

- January 2022. URL http://arxiv.org/abs/2102.11181 arXiv:2102.11181 [cond-mat, physics:physics].
- Amit Tzur, Ran Kafri, Valerie S. LeBleu, Galit Lahav, and Marc W. Kirschner. Cell Growth and Size Homeostasis in Proliferating Animal Cells. Science, 325(5937):167–171, July 2009. ISSN 0036-8075, 1095-9203. doi: 10.1126/science.1174294. URL https://www.science.org/doi/10.1126/science.1174294
- P. Van Liedekerke, M. M. Palm, N. Jagiella, and D. Drasdo. Simulating tissue mechanics with agent-based models: concepts, perspectives and some novel results. Computational Particle Mechanics, 2(4):401–444, December 2015. ISSN 2196-4378, 2196-4386. doi: 10.1007/s40571-015-0082-3. URL http://link.springer.com/10.1007/s40571-015-0082-3.
- Stylianos Varchanis, Simon J. Haward, Cameron C. Hopkins, Alexandros Syrakos, Amy Q. Shen, Yannis Dimakopoulos, and John Tsamopoulos. Transition between solid and liquid state of yield-stress fluids under purely extensional deformations. *Proceedings of the National Academy of Sciences*, 117(23):12611–12617, June 2020. ISSN 0027-8424, 1091-6490. doi: 10.1073/pnas.1922242117. URL https://pnas.org/doi/full/10.1073/pnas.1922242117
- Franck J. Vernerey. Transient response of nonlinear polymer networks: A kinetic theory. *Journal of the Mechanics and Physics of Solids*, 115: 230-247, June 2018. ISSN 00225096. doi: 10.1016/j.jmps.2018.02.018. URL https://linkinghub.elsevier.com/retrieve/pii/S0022509617310712
- Franck J. Vernerey, Rong Long, and Roberto Brighenti. A statistically-based continuum theory for polymers with transient networks. *Journal of the Mechanics and Physics of Solids*, 107:1–20, October 2017. ISSN 00225096. doi: 10.1016/j.jmps.2017.05.016. URL https://linkinghub.elsevier.com/retrieve/pii/S0022509617301874
- Tom Wyatt, Buzz Baum, and Guillaume Charras. A question of time: tissue adaptation to mechanical forces. Current Opinion in Cell Biology, 38:68-73, February 2016. ISSN 09550674. doi: 10.1016/j.ceb.2016.02.012. URL https://linkinghub.elsevier.com/retrieve/pii/S0955067416300199.
- Tom P. J. Wyatt, Andrew R. Harris, Maxine Lam, Qian Cheng, Julien Bellis, Andrea Dimitracopoulos, Alexandre J. Kabla, Guillaume T. Charras, and Buzz Baum. Emergence of homeostatic epithelial packing and stress dissipation through divisions oriented along the long cell axis. *Proceedings of the National Academy of Sciences*, 112(18):5726–5731, May 2015. ISSN 0027-8424, 1091-6490. doi: 10.1073/pnas.1420585112. URL https://pnas.org/doi/full/10.1073/pnas.1420585112
- Matthew A. Wyczalkowski, Zi Chen, Benjamen A. Filas, Victor D. Varner, and Larry A. Taber. Computational models for mechanics of morphogenesis. *Birth Defects Research Part C: Embryo Today: Reviews*, 96(2):132–152, June 2012. ISSN 1542975X. doi: 10.1002/bdrc.21013. URL https://onlinelibrary.wiley.com/doi/10.1002/bdrc.21013
- Guang-Kui Xu, Yang Liu, and Bo Li. How do changes at the cell level affect the mechanical properties of epithelial monolayers? *Soft Matter*, 11 (45):8782–8788, 2015. ISSN 1744-683X, 1744-6848. doi: 10.1039/C5SM01966D. URL http://xlink.rsc.org/?D0I=C5SM01966D.
- Guang-Kui Xu, Yang Liu, and Zhaoliang Zheng. Oriented cell division affects the global stress and cell packing geometry of a monolayer under stretch. *Journal of Biomechanics*, 49(3):401–407, February 2016. ISSN 00219290. doi: 10.1016/j.jbiomech.2015.12.046. URL https://linkinghub.elsevier.com/retrieve/pii/S002192901600004X.
- Le Yan and Dapeng Bi. Multicellular Rosettes Drive Fluid-solid Transition in Epithelial Tissues. *Physical Review X*, 9(1):011029, February 2019. ISSN 2160-3308. doi: 10.1103/PhysRevX.9.011029. URL https://link.aps.org/doi/10.1103/PhysRevX.9.011029
- Jennifer A Zallen and Eric Wieschaus. Patterned Gene Expression Directs Bipolar Planar Polarity in Drosophila. Developmental Cell, 6(3):343–355, March 2004. ISSN 15345807. doi: 10.1016/S1534-5807(04)00060-7. URL https://linkinghub.elsevier.com/retrieve/pii/S1534580704000607.
- Jian Zhou, Siladitya Pal, Spandan Maiti, and Lance A. Davidson. Force production and mechanical accommodation during convergent extension. *Development*, 142(4):692-701, February 2015. ISSN 1477-9129, 0950-1991. doi: 10.1242/dev.116533. URL https://journals.biologists.com/dev/article/142/4/692/47164/Force-production-and-mechanical-accommodation